LEVEL

Semiannual Technical Summary

Seismic Discrimination

3¹ March 1978

Lincoln Laboratory

MASSACHUSETTS INSTITUTE OF TECHNOLOGY

LEXINGTON, MASSACHUSETTS

D D C

AUG 10 1978

A

78 08 04 035

This technical report has been reviewed and is approved for publication.

FOR THE COMMANDER

Raymond L. Loiselle, Lt. Col., USAF
Chief, ESD Lincoln Laboratory Project Office

MASSACHUSETTS INSTITUTE OF TECHNOLOGY

LINCOLN LABORATORY

(6) **SEISMIC DISCRIMINATION.**

(10) Michael A. /Chinnery

(9) SEMIANNUAL TECHNICAL SUMMARY REPORT.

TO THE

DEFENSE ADVANCED RESEARCH PROJECTS AGENCY

(11) 31 mar 78

(12) 79 p.

1 OCT____77 — 31 MARCH 1978,

ISSUED 9 JUNE 1978

(15) F19628-78-C-ppp2, ARPA Order-512

(18) ESD (19) TR-78-64

D D C
RECEIVED
AUG 10 1978
A

LEXINGTON   MASSACHUSETTS

207650

78 08 04 035

ABSTRACT

This report describes 23 investigations in the field of seismic discrimination. These are grouped as follows: regional seismic studies (13 contributions), miscellaneous studies (6 contributions), and recent developments in our data and computer systems (4 contributions).

CONTENTS

SUMMARY

This is the twenty-eighth Semiannual Technical Summary report describing the activities of Lincoln Laboratory, M.I.T., in the field of seismic discrimination. This report covers the period 1 October 1977 to 31 March 1978. The objective of the Lincoln Laboratory program is to carry out fundamental research into the seismological problems associated with the detection, location, and identification of earthquakes and nuclear explosions, and with the estimation of explosion yields. In order to investigate these problems, we are continuously improving our ability to manipulate and process seismic data from a global network of high-quality digital stations and arrays.

During the present six-month period, we have concentrated mainly upon studying the nature of seismograms at regional distances (<2000 km) in the context of seismic discrimination. A variety of studies have investigated the utility of crustal body-wave phases and short-period surface waves in the detection, location, and discrimination of events at these distances.

We have compared locations of three nuclear explosions in Nevada, using crustal phases only, with those from teleseismic data only and found the accuracy of the epicenters obtained to be roughly equivalent, but that crustal-phase calibration may frequently be necessary. The utility of differential Pg-Pn travel times as a depth discriminant has been studied: it appears to work only at distances of less than 500 km. Crustal-phase travel-time data from NTS explosions have been used to calibrate the Basin and Range structural province. A study of film chip recordings of Soviet explosions has demonstrated that although Pn and Sn are readily identifiable, the other crustal phases are more difficult to identify. A comparison of broad-band and short-period recordings of regional events at the Albuquerque SRO seems to indicate some advantages in broad-band recording for discrimination purposes. Two sets of sonograms, one for the Western and the other for the Eastern U.S., show the viability of this technique in phase identification. Polarization filtering also appears to enhance phase identification at regional distances.

The Lg phase has been investigated for a variety of paths. Wavenumber spectra at NORSAR indicate that this very emergent feature of regional seismograms is mostly incoherent and due to scattering from more-coherent higher-mode Rayleigh waves of short duration. The propagation of Lg across Western Russia has been studied at both NORSAR and WWSSN stations in Scandinavia: it appears to be transmitted quite efficiently across this region, with no anomalous attenuation due to either the Ural mountains or the Baltic Sea.

Amplitude-distance curves for various crustal phases have been determined for Eastern North America and applied to a larger dataset, including Soviet explosions, for magnitude determination. A magnitude scale based on Lg amplitudes appears to have some utility as a discriminant when compared with body-wave magnitudes.

Several studies involving teleseismic data also have been carried out. A preliminary assessment of the utility of ocean-bottom seismometers for seismic discrimination purposes has been carried out. The seafloor appears likely to provide low-noise sites for surveillance of previously inaccessible regions, and recent technical developments make adequate seismometer deployment there quite feasible. A separate study of ocean-ridge earthquakes shows that their locations can be considerably improved with ray-tracing procedures in a realistic ocean-ridge model. A method for the extension of ellipticity corrections to surface-reflected phases is

described. A study of P-wave velocity in the Tonga deep-earthquake zone shows a correlation of the major anomalous velocity region with a sudden shear strain increase. Analysis of Meshed SRO long-period recordings of a double explosion indicates that events separated by as little as 20 sec can be separated in the surface-wave train. The spectral characteristics of events in an aftershock sequence have been studied using SRO data: seismic scaling effects are readily observable.

We continue to develop our data-handling facilities. A 300-Mbyte disk has greatly increased our on-line storage capability. System software, particularly that to handle Datacomputer interaction, has been substantially improved. The seismic display package has now been implemented.

<div align="right">M. A. Chinnery</div>

I. REGIONAL SEISMIC STUDIES

A. THE USE OF CRUSTAL PHASES IN LOCATING EXPLOSION EPICENTERS

We relocated the Greeley, Scroll, and Rulison explosions using combinations of the available data set of arrival times in an attempt to evaluate the usefulness of crustal-phase observations. Our data sets for Greeley and Scroll consisted of all the arrival times reported in the ISC Bulletin complemented by additional crustal-phase arrival times in the 0 to 10° range. For Rulison, we had only the ISC data. It was necessary to read these latter arrival times from the LRSM film because there were no S phases listed in the shot reports. A fortuitous advantage to our procedure was uniformity of observation, since all the events were read by one analyst. In order to use all the data for each event in a single location, we assigned the errors of observation given in Table I-1 to the various phases. The effect of this was to reduce the dependence of the epicenter on arrival times, which cannot be read as accurately as the first arrivals.

TABLE I-1	
ESTIMATED ERRORS OF OBSERVATION	
Phase	Error (sec)
P	0.5
Pn	1.0
S	1.0
Sn	1.0
PKP(DF)	1.0
Pg	3.0
P*	3.0
Sg	3.0
S*	3.0
PP	5.0
PcP	5.0

The ISC epicenters for these events are plotted in Fig. I-1. Greeley and Scroll were 825- and 20-kt shots detonated at NTS. Rulison was a 40-kt gas stimulation experiment detonated in Colorado. Since the crustal structures vary between these two source regions, we expect to find the contribution of the crustal-phase arrival times sensitive to the layer parameters.

The epicenter locations were done using the Jeffreys-Bullen travel-time tables for teleseismic arrivals, and either the JB tables or our own Basin and Range tables (see Sec. C below) for the crustal-phase arrivals. In each case, the depth was constrained to that given in the shot report. Jeffreys' method of "uniform reduction" was used to reduce the effect of erroneous data

values. To our knowledge, these procedures are essentially the same as those used by the USGS and ISC Bulletins.

The results of a variety of location experiments are given in Tables 1-2 to 1-4. They generally tend to show that a large amount of data in the regional distance range gives epicenters as accurate as those derived from a large amount of teleseismic data. On the other hand, adding a few good regional stations to a teleseismic data set usually improves the resulting epicenter both in accuracy and quality. The results for Rulison were not as good as those for Greeley and Scroll. We feel that this is due to our having to rely on tabulated crustal-phase arrival times, and the Colorado plateau crust differing from either our Basin and Range structure or that implied by the JB tables.

The following general conclusions also follow from our data. Of the six possible crustal phases, only Pn is reliable enough to use in epicenter locations. The others are useful primarily for determining crustal structure. The accuracy of crustal-phase locations is directly dependent on how well the crustal velocity structure is known. In unfamiliar regions, the crust will have to be "calibrated" in order to use near-in stations for location work. Finally several of the results given in Tables I-2 through 1-4 seem to show high quality but inaccurate epicenters. These appear to reflect bias in the travel-time tables which should be eliminated either by "calibration" or relative event-location techniques. If the existence of a well-recorded master event in a region can be assumed, then substantial improvements to our results may be possible.

<div align="right">

D. W. McCowan
R. E. Needham

</div>

B. Pg – Pn TRAVEL TIMES FOR NTS EXPLOSIONS

Figure I-2 is a plot of 142 Pg minus Pn travel times for NTS explosions recorded by LRSM stations mainly in the Basin and Range province. The two lines on the plot are the theoretical zero depth Pg – Pn time from McCowan and Needham[1] and an empirical line from Ryall.[2] The theoretical line is based on the following plane layered Basin and Range model:

Layer	Thickness	P-Velocity
1	15	6.03
2	18	6.73
3	∞	7.88

The equations are:

$$t \equiv t(Pg) - t(Pn) = \frac{\sqrt{x^2 + h^2}}{V_1} - \frac{x}{V_3} - \frac{h \tan\phi_1}{V_3} + \frac{h}{V_1 \cos\phi_1} - A$$

$$A = \frac{2D_2 \tan\phi_2}{V_3} - \frac{2D_1 \tan\phi_1}{V_3} + \frac{2D_2}{V_2 \cos\phi_2} + \frac{2D_1}{V_1 \cos\phi_1} = 6 \text{ sec}$$

where $\sin\phi_1 = V_1/V_3$ and $\sin\phi_2 = V_2/V_3$. In these equations, h is the source depth and x is the distance, both in kilometers.

<div align="center">

2

</div>

TABLE 1-2
GREELEY LOCATION EXPERIMENT

Stations	Latitude (°N)	Longitude (°W)	Depth (km)	Confidence Ellipse Area (km²)	Mislocation	No. of Observations
Greeley hypocenter	37.30	116.41	1.2	-	-	-
All ISC data	37.39 ± 0.01	116.32 ± 0.01	1.0g	2.51	13.0	221
All data <10°	37.28 ± 0.02	116.35 ± 0.02	1.0g	9.34	5.3	50
All data <20°	37.31 ± 0.01	116.30 ± 0.02	1.0g	5.03	10.0	77
All data >20°	37.51 ± 0.01	116.35 ± 0.01	1.0g	3.11	23.8	235
All data >30°	37.40 ± 0.01	116.25 ± 0.01	1.0g	3.96	5.3	112
MN-NV, KN-UT, MO-ID, FK-CO, TFO	37.41 ± 0.04	116.19 ± 0.03	1.0g	30.35	23.1	22
MN-NV, KN-UT, MO-ID, FK-CO	37.32 ± 0.06	116.25 ± 0.02	1.0g	42.85	14.4	17
MN-NV, KN-UT, MO-ID	37.43 ± 0.05	116.17 ± 0.04	1.0g	47.12	25.8	12
All data >20° + MN-NV, KN-UT, MO-ID, FK-CO	37.40 ± 0.01	116.37 ± 0.01	1.0g	2.51	11.8	250
All data >20° + MN-NV, KN-UT, MO-ID	37.40 ± 0.01	116.37 ± 0.01	1.0g	2.51	11.8	245
All data >20° + MN-NV, MO-ID	37.40 ± 0.01	116.37 ± 0.01	1.0g	2.51	11.8	241
All data >20° + MN-NV	37.41 ± 0.01	116.38 ± 0.01	1.0g	2.51	12.5	236

TABLE I-3

SCROLL LOCATION EXPERIMENT

Stations	Latitude (°N)	Longitude (°W)	Depth (km)	Confidence Ellipse Area (km²)	Mislocation	No. of Observations
Scroll hypocenter	37.34	116.38	0.22	–	–	–
All ISC data	37.34 ± 0.02	116.40 ± 0.03	0.0g	12.52	2.7	30
All data <10°	37.32 ± 0.02	116.35 ± 0.03	0.0g	15.17	3.7	3ε
All data <20°	37.32 ± 0.02	116.35 ± 0.03	0.0g	15.17	3.6	62
All data >20°	Not Enough Stations			–	–	–
All data <30°	37.36 ± 0.01	116.24 ± 0.02		5.72	12.8	64
STAS MN-NV, EY-NV, KN-UT, CP-CA	37.30 ± 0.02	116.18 ± 0.03	0.0g	27.77	18.4	16
STAS EY-NV, KN-UT, CP-CA	37.28 ± 0.0ε	115.90 ± 0.05	0.0g	49.26	43.1	13
All data >20° + MN-NV, EY-NV, KN-UT, CP-CA	37.34 ± 0.03	116.20 ± 0.03	0.0g	28.27	16.1	18
All data >20° + EY-NV, KN-UT, CP-CA	37.32 ± 0.03	115.94 ± 0.05	0.0g	46.75	39.1	15
All data >20° + EY-NV, CP-CA	37.45 ± 0.05	116.86 ± 0.19	0.0g	180.52	44.3	11
All data >20° + CP-CA	37.5ε ± 0.06	116.99 ± 0.21	0.0g	309.23	50.2	5

TABLE 1-4
RULISON LOCATION EXPERIMENT

Stations	Latitude (°N)	Longitude (°W)	Depth (km)	Confidence Ellipse Area (km²)	Mislocation	No. of Observations
Rulison hypocenter	39.41	107.95	2.57	-	-	-
All ISC data	39.54 ± 0.01	107.84 ± 0.01	3.0g	3.02	17.4	112
All data < 10°	39.34 ± 0.02	107.87 ± 0.02	3.0g	11.22	10.5	55
All data < 20°	39.55 ± 0.01	107.77 ± 0.01	3.0g	3.39	22.0	84
All data > 20°	39.50 ± 0.02	108.04 ± 0.02	3.0g	10.56	12.8	74
All data < 30°	39.55 ± 0.01	107.95 ± 0.01	3.0g	2.42	19.2	104
TFO, BMO, MCN, LEE, KN-UT	39.33 ± 0.05	108.39 ± 0.01	3.0g	291.01	39.0	9
TFO, MCN, LEE, KN-UT	38.95 ± 0.11	108.72 ± 0.20	3.0g	599.23	83.7	8
TFO, LEE, MCN	39.00 ± 0.11	108.61 ± 0.21	3.0g	643.65	73.0	6
All data > 20° + TFO, MCN, LEE, KN-UT	39.52 ± 0.02	107.95 ± 0.02	3.0g	7.76	12.3	78
All data > 20° + TFO, MCN, LEE	39.52 ± 0.02	107.95 ± 0.02	3.0g	7.76	12.3	77
All data > 20° + TFO, MCN	39.52 ± 0.02	107.96 ± 0.02	3.0g	8.80	12.3	76
All data > 20° + TFO	39.51 ± 0.02	107.97 ± 0.02	3.0g	9.24	11.4	75

The partial derivatives evaluated at zero depth are:

$$\left.\frac{\partial t}{\partial x}\right|_{h=0} = 0.0389 \ \text{sec/km}$$

$$\left.\frac{\partial t}{\partial h}\right|_{h=0} = 0.106 \ \text{sec/km} \quad .$$

In other words, this discriminant is almost three times more sensitive to depth than it is to distance. On the other hand, observational errors of 0.1 sec limit the potential depth resolution to 3 km. Achieving this depth resolution would require locations to be known within 1 km. These estimates, of course, assume that the layer parameters are constant and known. Ryall's line[2] is based on NTS explosion and Nevada earthquake data out to a 300-km distance. Our data show substantial numbers of explosions above the line in the 250- to 300-km range. Unfortunately, Ryall's line falls increasingly away from the data population beyond 300 km. In this regard, the theoretical zero depth line follows the data population but also illustrates the increasing scatter with distance.

Our conclusion is that Pg -- Pn travel time may be a discriminant at short distances but errors, possibly structurally dependent, play a dominant role beyond 500 km. The cause of these errors should be studied so that they can be eliminated in the data analysis.

<div align="right">
D. W. McCowan
R. E. Needham
</div>

C. CALIBRATION OF THE BASIN AND RANGE WITH NTS CRUSTAL-PHASE DATA

We reread the LRSM short-period film to enlarge the data set of crustal-phase travel times. After limiting ourselves to 20 NTS shots and 34 LRSM stations in the Basin and Range (BR) province, we had 72, 20, 74, 39, 23, and 32 Pn, P*, Pg, Sn, S*, and Sg arrival times, respectively. From these, we determined the two-layer Basin and Range structure given in Table I-5. Figures I-3 to I-8 show the corresponding travel times from our model plotted along with the data.

TABLE I-5 BASIN AND RANGE AND JEFFREYS-BULLEN MODEL PARAMETERS						
Layer	BR h (km)	JB h (km)	BR P (km/sec)	JB P (km/sec)	BR S (km/sec)	JB S (km/sec)
1	15.2	15.0	5.01	5.57	3.53	3.37
2	19.4	18.0	6.55	6.50	3.73	3.74
3	∞	∞	7.86	7.85	4.43	4.42

It appears from these data that the JB crustal model is an excellent approximation to the Basin and Range except in the first layer. Our first-layer velocities are 8- and 5-percent higher for P and S, respectively. Furthermore, the Basin and Range does appear to be well modeled by a two-layer crust as far as crustal-phase travel times are concerned.

<div align="right">
D. W. McCowan
R. E. Needham
</div>

D. CRUSTAL PHASES FROM SOVIET PNEs RECORDED AT WWSSN STATIONS

We have studied WWSSN short-period recordings in the distance range 2° to 16° from 14 PNEs in Western Russia in an attempt to determine some of the characteristics of propagation and source effects in this area. The events and paths used are shown in Fig. I-9. An experienced analyst picked as many phases as possible, without recourse to travel-time tables, and the resulting suite of 185 time picks from 35 seismograms is shown in Fig. I-10. We attempted to associate seismic phases with as many of these time picks as possible, using as a basis a model determined by Massé[3] for the Canadian Shield. We generated travel-time curves for the crustal phases Pn, Sn, P*, S*, Pg, and Sg and assigned any time pick falling within 4 sec (for P) or 8 sec (for S) of the given travel time to the particular phase. We were able to identify 35 Pn, 32 Sn, 16 Pg, 13 Sg, 12 P*, and 8 S* in this manner. A further 20 arrivals were identified by the analyst as the phase Lg from their duration and character. Thirty-nine (21 percent) of the arrivals could not be identified with the above crustal phases and were probably associated with upper-mantle refractions with apparent surface velocities of 8.5 or greater: One of these (10.4 km/sec) was clearly identifiable and corresponds to one observed by Massé and Alexander[4] in the same region. We believe that our results show

    (1)   that a shield model is appropriate for the paths studied,

    (2)   that Pn and Sn can almost always be identified and measured,

    (3)   that the other crustal phases are more difficult to identify, and

    (4)   that a trained analyst can pick times for phases prior to identification with a false-alarm rate of less than 20 percent.

For every time pick made, an amplitude (peak-to-peak) was also measured except where off scale, and reduced to ground motion at the station. For none of the events were there sufficient stations to permit construction of an amplitude distance curve, and we therefore reduced the amplitudes for each event by a scale factor related to the ISC m_b through

$$\text{Reduced Amplitude} = (\text{Recorded Amplitude}) \times (5.0 - m_b)$$

i.e., to the amplitude from an event of $m_b = 5.0$. Amplitude-distance curves were plotted for each phase: the results were uniformly hopeless and are not shown here.

For comparison with the other studies included in this report, we have determined amplitude ratios of (Pn/Lg), (Sn/Lg), and (Sn/Pn), shown in Fig. I-11. Some rather dubious identifications of Lg are included here; in some cases only an upper limit to its amplitude could be determined and thus only a lower limit to the ratios (Sn/Lg) and (Pn/Lg) determined. These are indicated by arrows in Fig. I-11. These ratios may be of some use as a discriminant, but, since we have studied explosions only, they are included here purely as an indication of the nature of explosion seismograms in this region. Some of these ratios have been included in a study (elsewhere in this report) of explosion and earthquakes in the Canadian Shield, or similar regions.

<div align="right">

R.G. North
L.C. Lande

</div>

E. CRUSTAL PHASES RECORDED ON SRO SHORT-PERIOD AND BROAD-BAND SYSTEMS

Crustal phase Pn, Pg, and Lg recorded on the broad-band SRO system at Albuquerque are compared with the corresponding records from a short-period vertical SRO. It should be noted

| TABLE I-6 |
| EVENT PARAMETERS FOR SRO BROAD-BAND RECORDED EVENTS |

Date	15 September 1977	27 September 1977	30 September 1977
Origin	14:36:30.1	14:00:00.2	10:19:19.6
Latitude (°N)	37.033	37.151	40.51
Longitude (°W)	116.043	116.068	110.28
Depth	0	0	5
Mb	4.5	4.8	5.0
Location	NTS	NTS	Utah
Distance	8.03	8.07	6.33
Azimuth	287.88	288.67	332.66
Figure	I-16	I-17	I-18

that the records came from separate recording systems located at the Albuquerque Seismic Laboratory. Record pairs from two NTS shots and a Utah earthquake are shown in Figs. II-12(a) and (b). The bottom record of each pair is from the short-period SRO. The onset of the Pn phase, the first arrival, from first explosions failed to trigger the event detector for the short-period SRO; consequently, this record is not complete. Each event is located about 8° from Albuquerque with the great-circle path more northwesterly for the earthquake. The event parameters are listed in Table I-6.

From the analog records, the advantages of broad-band recording, if any, can not be seen. However, comparison of power spectra shows that longer-period signals that are preferentially excited by the earthquake are suppressed by the short-period SRO system. This can be seen in Figs. II-13(a) and (b) by comparing the Lg spectra in the bandpass from 0.2 and 0.3 Hz. The Lg power is about 10 dB above the noise level on the short-period SRO, and about 20 dB above the noise level on the broad-band record. This disparity is consistent with the 12-dB/octave slope in the amplitude response of the short-period SRO which is symmetrical about a peak frequency of 1 Hz (Ref. 5). The broad-band Pg signal is also richer in longer-period energy.

All power spectra were computed from 512 data points which correspond to about 26 sec of record at the digitizing rate of 20 samples/sec. Zeros were used to pad out the time windows of signals with durations less than 512 points. Some Pn and Pg time windows (Figs. I-12) were significantly shorter than 26 sec, with the result that ratios of signal-to-noise power inferred from Figs. I-13 and I-14 are underestimates by a factor of 2 to 4. A cosine taper was used to smooth the spectral estimates.

A comparison of the power spectra from the NTS shots reveals only a marginal increase in longer-period energy in the broad-band recordings. Spectra from the larger of these shots are shown in Figs. I-14(a) and (b). Spectra from a small Colorado earthquake (not shown in Figs. I-12)

revealed significant energy above the Nyquist frequency of 10 Hz. Aliased energy like this is expected to be a greater problem where transmission paths are more efficient such as those that cross shield regions or stable platforms.

<div align="right">T. J. Fitch
R. M. Sheppard</div>

F. SONOGRAMS OF SRO BROAD-BAND RECORDED EVENTS

The second SRO seismometer located at the Albuquerque, New Mexico SRO site has been modified to record broad-band data directly from the output of the instrument. These signals are the raw seismometer outputs and are not filtered in any manner. Recording of the data is achieved by treating the signals as if they are the short-period data and thereby recording the data in the normal position on tape that is usually occupied by the short-period data. Both the horizontal and the vertical outputs are recorded at 20 Hz. When treated in this fashion, the recording and analysis of the data can be done with most of the existing computer programs.

Several well-recorded events have been analyzed for the frequency content in the signal. Three excellent examples of these events will be discussed here. The first two events are underground nuclear explosions at the Nevada test site, and the third event is an earthquake located in Utah. The event parameters are given in Table I-6.

Figure I-15 shows the relative distribution of the event locations with respect to ANMO. Figures I-16, I-17, and I-18 are sonogram plots (frequency vs time) of the explosions and the earthquake described in Table I-6. In these figures, the vertical axis represents frequency and the horizontal axis is relative time. A sonogram therefore is a representation of the frequency content of a signal vs time. To achieve these figures, the event signal is first filtered by 31 constant-Q filters, then the 31 outputs are integrated over 1-sec intervals, and, finally, the values are contoured into a sonogram. The black areas of the figures represent the areas of peak signal, while the hatched areas are those regions which are 6 dB down (1/4 amplitude lower) from the peak signal. The heavy solid black lines indicate areas which are 12 dB lower than the peak areas. Each figure displays the 3 components, Z, N-S, and E-W, of the ANMO broad-band seismometer (except Fig. I-16 which did not record the N-S component).

The areas of interest in Figs. I-16 through I-18 lie in the frequency distribution of the surface waves. The two explosions exhibit a more confined or limited frequency distribution than does the earthquake. One might expect that the explosion would contain fewer high frequencies in the surface-wave train than does the earthquake, since the shots are 2° further from ANMO than the earthquake. However, there seems to be a wider distribution of frequencies for the earthquake than one would expect from just a 2° increase in distance. This wider frequency distribution is also evident over the entire waveform of the earthquake. It is evident from these figures that a discriminant based on spectral ratio of the surface-wave train would discriminate these three events. However, further analysis is continuing on this potential discriminant using broad-band data.

<div align="right">R. M. Sheppard</div>

G. SONOGRAMS FOR AN EASTERN U.S. LRSM PROFILE FROM THE NUCLEAR EXPLOSION SALMON

We analyzed an east coast profile of LRSM 3-component short-period recordings of the SALMON explosion by the sonogram process. The explosion and station locations are shown in Fig. I-19. The sonogram output is a series of energy contours over a frequency-vs-time

					TABLE I-7		
				SALMON CRUSTAL-PHASE DATA			
Station	Δ (km)	Δ (deg)	Phase	Travel Time	Frequency (Sonogram)	Frequency (Shot Report)	Amplitude (mμ)
EU-Al	242	2.18	Pn	36.5	3.0	4.0[†]	370[†]
			P*	39.5	3.0	–	197
			Pg	42.5	3.0	3.3[†]	474[†]
(SPZ)			Sn	67.5	2.6	–	570
(SPZ)			Lg	73	2.0	2.5[†]	450
BL-WV	1058	9.59	Pn	129.2	2.6	2.5?[†]	5.12?[†]
			Pg	173.3	2.1	2.5[†]	29.2[†]
(SPT)			Sn	257.1			43
(SPT)			Lg	300.7		2.0[†]	45
BR-PA	1375	12.4	P	176.1	2.8	3.0[†]	11.5[†]
(SPT)			Lg	388		1.1[†]	91.2[†]
(SPT)			Sn	301.5			45
DH-NY	1795	16.2	P	225.0	2.1	2.5[†]	3.55[†]
(SPT)			Lg	503		1.1[†]	66.4[†]
LS-NH	2121	19.1	P	265.5			
(SPT)			Lg	595		1.0[†]	49.7[†]
HN-ME	2497	22.5	P	298.3	1.0	1.1[†]	17.5[†]
(SPZ)			Lg	705		1.3[†]	28
(SPZ)			Sn	518			15
SV2QB	3192	28.7	P	358.0[†]	2.1	2.0	5.8[†]

[†]Indicates values taken from the shot report.

coordinate system. The time axis is equivalent to group velocity if the distance to the event is known. In our implementation, the output is produced by applying a suite of constant-Q, narrow-band filters. Since these are recursive time-domain operators, there is a significant group delay between arrivals on the seismogram and energy contours on the plots.

The SALMON explosion was detonated in Mississippi and, in our case, observed along the whole east coast from 2.18° to 28.7° distance. It is thought that the Eastern U.S. is more representative of the Eurasian shield and platform areas than the Western U.S. It is, at least, a high-Q thick-crust region that propagates diagnostic phases like Lg in contrast to the Basin and Range province where Lg is difficult to observe. Unfortunately, there are several different geologic environments along this profile with different crustal structures. The explosion and the nearest station, EU-AL, are in the Gulf Coast plains. The intermediate stations, BL-WV, BR-PA, and DH-NY, are on the eastern plateau. The furthest stations, LS-NH and HN-ME, are on the New England plateau. One last station, SV2QB, which is not a part of the profile is on the Canadian Shield. Consequently, we expect a substantial scatter in observed amplitudes and periods with distance.

As noted by Alexander,[6] the obvious advantage to the sonogram process is that patterns of energy distribution can be identified which would be lost in simple amplitude and period measurements. From these, empirical discriminants like spectral ratios can be inferred and defined over frequency-time intervals. Representative sonograms for stations EU-AL, BR-PA, and DH-NY are shown in Figs. I-20 to I-22, respectively. The data interval for station EU-AL is unique because it includes all arrivals from the first P wave through the surface-wave train.

The results obtained by means of these energy distribution plots are listed in Table I-7, along with some taken from the SALMON shot report. We were able to identify several crustal body-wave and S-wave phases which were not given in the shot report. Sn-to-Lg ratios measured off the seismograms after the phases were identified varied from 1.25 at EU-AL to 0.54 at HN-ME.

Our conclusion is that the sonogram process is a useful tool for identifying seismic phases from their energy distributions in the frequency-time domain and that it should be applied to data from more regions as it becomes available.

<div align="right">D. W. McCowan</div>

H. POLARIZATION FILTERING OF THE FIRST ARRIVALS FOR THE EASTERN U.S. LRSM PROFILE FROM SALMON

Polarization filtering has been used to aid the analysis of the LRSM profile of seismic data from the U.S. explosion SALMON described above in Sec. G. Figures I-23(a) and I-24(a) show the 3-component data from EU-AL to HN-ME ranging from $\Delta = 2.2°$ to 22.5°. The data have been rotated toward the SALMON epicenter, and phase-free hi-pass filtered with a 6-dB cutoff of 0.8 Hz to remove microseisms. The times have been reduced in the figure by an amount $\Delta/10$ sec, to better align high-velocity phases.

A three-dimensional polarization scheme was used to enhance planar elliptical motion, e.g., isolated surface and body waves, while rejecting ellipsoidal data in which all three axes are comparable. The least-squares ellipsoid of motion with axes $l_1 > l_2 > l_3$ is calculated in a moving window of data, and the two largest axes, l_1 and l_2, are projected onto the data components. This amounts to truncating the data expansion to the two most-significant vector components out of three, and results in a considerable "cleaning up" of 3-component data.

<div align="center">11</div>

The projected data are further scaled by a gain factor which depends on the instantaneous ellipticity ϵ defined by

$$\epsilon = \sqrt{2}\ell_3/(\ell_1^2 + \ell_2^2)^{1/2} \qquad 0 \leqslant \epsilon \leqslant 1$$

where

$$0 \leqslant \epsilon \leqslant 1 \quad .$$

Since $\ell_3 < \ell_2 < \ell_1$, ϵ is nearly 0 when $\ell_3 \ll \ell_2$. This case occurs when the data are polarized in the plane of an ellipse with axes ℓ_1 and ℓ_2. As ℓ_3 becomes larger, ϵ approaches 1 in the case of spheroidal motion, i.e., where $\ell_1 = \ell_2 = \ell_3$. In order to reject spheroidal motion, in the least-squares sense and enhance elliptical motion, a Butterworth-type ellipticity filter was used as the gain factor given by

$$g = 1/[1 + (\epsilon/\epsilon_0)^{2n}]^{1/2} \quad .$$

This gain factor is a low-pass filter which approaches 1 as $\epsilon \to 0$ and decreases 6n dB/octave above the cutoff value ϵ_0. Parameters n and ϵ_0 are arbitrary.

In Figs. I-23(b) and I-24(b), the polarized data are shown displayed under the original data. For this processing, the cutoff ellipticity was $\epsilon_0 = 0.25$, the filter order was n = 3, and the moving time window for the ellipsoid calculations was 1 sec wide. Comparing these figures, one sees that the polarization filtering sharpens the arrivals and extracts a number of unknown phases, compressional and shear.

A detailed analysis of all the enhanced arrivals is not possible without a closely spaced network of stations as used, for example, in the Early Rise experiment.[3]

Clearly, polarization methods can be useful for near-regional problems in discrimination, but good-quality 3-component data must be obtained. Detailed analysis of complex crustal phases cannot be attempted with a sparse network, and a dense network seldom yields unambiguous geophysical results.

<div style="text-align:right">C. W. Frasier</div>

I. THE MECHANISM OF Lg PROPAGATION

Press[7] lists the maximum horizontal Lg to maximum vertical Rg amplitude ratio as a possible discrimination parameter. On theoretical grounds, it is reasonable to expect the ratio to be significantly greater for earthquakes than for explosions due to the relative distribution of shear and compressional energy between the two sources and the suspected nature of Lg. Indeed, Bath[8] gives the measured ratio as 2:1 to earthquakes and 0.8 for explosions. These figures have not been established for statistical quantities of events, and earthquakes that violate the discriminant can be found. The problem may lie in our poor understanding of the nature of Lg — its generation, its propagation, and its observed structure. To better understand Lg, its spatial and temporal behavior over NORSAR subarrays has been investigated.

Briefly, Lg is observed over continental source-receiver paths as a short-period large-amplitude wave with an average source-receiver velocity of about 3.5 km/sec. Most of its motion is transverse, though an appreciable vertical component is present. The phase is extremely emergent, often building up over several minutes before peaking. Figure I-25 shows the the seismogram recorded on the NORSAR short-period vertical (SPV) instrument at location 01B0

for the event listed in the PDE as 4 October 1971 at 10:00:02.0 at 61.6°N and 47.1°E (Western Russia) of magnitude 5.1 m_b. The event is presumed to be an underground explosion. It measures 17.4° from NORSAR with a great-circle back azimuth of 65°. The bottom scale shows source-receiver group velocities. At a velocity of 3.5 km/sec (marked by Lg), there is a local maximum following a continual buildup of energy beginning approximately 3 min. before. The data lie in the band 0.5 to 2 Hz. Figure I-26 shows the records at each element of the 1B subarray. While there is coherence in the envelope, small-scale coherence is low.

The wavenumber spectra[9] of several time sections of these records were examined to determine the portion of coherent energy and the direction and phase velocity of its propagation. The intervals studied were: the first arrival, 1 min. after the first arrival, 2 min. prior to the maximum Lg time, at the maximum Lg time, immediately after the maximum Lg time, and 1 min. past the Lg time. Of these intervals, only the first arrival and the section immediately after the maximum Lg time (but not including it) showed any appreciable wavenumber coherence in the source direction. The wavenumber spectra for these two periods are shown in Figs. I-27 and I-28. Accordingly, the vertical component of the Lg phase for this event as recorded at NORSAR may be described as follows: a steady buildup of essentially spatially incoherent energy peaking at a group velocity of 3.5 km/sec, followed by a coherent wave train of time duration less than 25 sec arriving from the direction of the source with phase velocity 4.1 km/sec, followed by diminishing incoherent motion.

The above observations are consistent with the interpretation of the vertical part of Lg (Ref. 9) as second- and/or higher-mode Rayleigh waves, with the bulk of their energy confined to a part of the upper crust (but not at the surface), and the emergent and diminishing parts, including the maximum trace amplitude, being scattered waves. The consequence of such behavior is that the amplitude in the scattered portion of the phase is not only a function of size of the propagating wave but also of the scale of inhomogeneity in the crust near the receiver. The amplitude of the propagating part of the phase would be the integrated effect of spreading and scattering over the entire path. Under these circumstances, the usefulness of Lg for regional detection, location, and discrimination purposes would be enhanced by employing small arrays and spatial processing that could separate path, source, and receiver characteristics.

<div align="right">T. E. Landers</div>

J. Lg MEASUREMENTS AT NORSAR FROM SOVIET EXPLOSIONS AND TWO EARTHQUAKES

We have investigated the available short-period data from NORSAR in an attempt to calibrate Lg propagation across Western Russia, and to determine if topographic features such as the Urals, the Barent Seas, and the Baltic Sea are barriers to this propagation. These data complement another study by R. G. North (Sec. D above) which used WWSSN stations, and the results obtained here are similar. Table I-8 is a list of the usable events which had long enough data windows after the first P arrivals to include detectable Lg phases. All events except those with nonzero depth are explosions.

Figure I-29 shows the ISC epicenter locations, m_b values, and dates of the events on which we measured phases. Seismograms of the events were searched for emergent Lg arrivals with group velocities between about 3.5 to 3.6 km/sec. The envelope peaks were measured where the energy was clearly above the noise before the P arrival, and isolated by obvious changes in noise and frequency character before and after the Lg phase. Although the amplitudes are

				TABLE I-8				
			NORSAR EVENTS FOR WHICH Lg TIME WINDOWS WERE AVAILABLE; EXPLOSIONS HAVE ZERO DEPTH					
		Location					Lg	
Event	Date	(°N)	(°E)	m_b	h	Delta	Seen	Lg Amplitude
1	12/22/71	47.87	48.22	6.0	0	24.95	Barely	388
2	10/04/71	61.61	47.22	4.6	0	17.35	Yes	105
3	04/16/72	47.79	16.04	4.7	18	13.40	Yes	664
4	06/17/72	48.40	14.52	4.6	20	12.63	Yes	64
5	07/09/72	49.78	35.40	4.8	0	17.73	Yes	108
6	09/30/73	51.66	54.54	5.2	0	25.6	Good	195
7	10/26/73	40.84	48.29	4.4	41	30.27	No	—
8	08/14/74	68.94	75.83	5.4	0	27.45	Yes	80
9	08/29/74	67.23	62.10	5.0	0	22.74	Yes	78
10	09/13/74	49.76	78.03	5.2	0	38.11	Maybe	<25 (noise)

TABLE I-9

NORSAR TIME-DOMAIN MEASUREMENTS

	Event	P (biggest arrival in first 20 sec)				Lg Amplitude (mµ)	Period	Lg/P Amplitude Ratio
		m_b	Distance (deg)	Amplitude (mµ)	Period (sec)			
Earthquakes	3	4.7	13.4	147	1.0	664	1.6	4.52
	4	4.6	12.6	34	1.0	64	0.8	1.88
PNEs	5	4.8	17.7	336	0.4	108	0.9	0.32
	2	4.6	17.3	254	0.3	105	0.7	0.41

probably accurate to within a factor of 2 across the NORSAR array, it must be emphasized that arrival times are very suspect and cannot be considered accurate for location purposes to within ±30 sec in most cases.

Two PNEs in Western Russia and two Austrian earthquakes are closest to NORSAR. The initial P waves of the two PNEs are much richer in high frequencies than the P waves of the Austrian earthquakes. Although the Austrian earthquakes are 4° to 5° closer to NORSAR than the PNEs, the structural paths are more complex and it is uncertain how much of the high-frequency-explosion energy is simply passed by the high-Q Baltic shield and Russian platform. The Lg phases for all four events are very emergent and complex in character with little coherence from sensor-to-sensor. This visual lack of coherence occurs even across the sensors of individual subarrays at NORSAR. Using high-resolution wavenumber analysis, however, Landers has separated the scattered from the direct waves in the Lg waveform (see Sec. I above).

Time-domain measurements picked on single NORSAR sensors for these four events are summarized in Table I-9. We note that the two earthquakes have inconsistent P and Lg amplitudes even though the m_b and locations are nearly identical. This is probably due to different source radiations along the takeoff direction to NORSAR. The PNE amplitudes seem more consistent even though their locations are widely separated. Lg/P amplitude ratios are 1.9 to 4.5 for the earthquake pair, whereas the PNE ratios are very consistent − 0.32 and 0.41.

In Fig. I-30 the spectra of a 20-sec P window and a similar length Lg window are displayed for the Austrian earthquake (event 3), which has the largest Lg/P amplitude ratio. Figure I-31 shows similar spectra for a PNE (event 5). The high-frequency character of the explosion P wave and the low amplitude of the Lg spectrum verify the time-domain observations.

Measurements of Lg amplitude for these four events and the remainder of the PNEs in Fig. I-29 are plotted vs distance from NORSAR in Fig. I-32. The amplitudes have been normalized to m_b 6.0. The dashed trend line is Nuttli's theoretical curve[10] for Lg decay with distance for earthquakes in the Eastern U.S., which besides geometrical spreading includes attenuation with distance given by $\exp[-0.07\Delta]$, where Δ is measured in degrees. This curve has been shifted vertically to pass through the level of scaled Lg amplitudes for the PNEs. The solid curve above the data is Nuttli's empirical formula for Lg amplitude vs distance from an m_b 6.0 earthquake. This comes from the relation between short-period, surface-wave amplitude and m_b given by

$$m_b = 1.66(\log \Delta) + \log(A/T)$$

where A is measured in millimicrons on a vertical short-period instrument.

From Fig. I-32 we see two interesting trends of the Lg data. First of all, there is no clear effect on Lg transmission of any topographic features in Fig. I-29 such as the Ural Mountains or the Barent Sea. The variation of Lg amplitude with distance from NORSAR seems to fit Nuttli's theoretical trend for the Eastern U.S. Secondly, the general level of Lg phases for PNEs when scaled to m_b 6.0 have a trend at least a magnitude unit below that expected for earthquakes in the Eastern U.S. This is a short-period observation analogous to the m_b:M_s criterion which works effectively for large events at teleseismic distances. Clearly, many earthquakes from Russia are needed to investigate the use of Lg as a discriminant. The data from the two coincident Austrian earthquakes are quite ambiguous and remind us that short-period surface waves are probably as sensitive to source radiation effects as are short-period body waves.

C. W. Frasier
R. M. Sheppard

15

K. PROPAGATION OF THE Lg PHASE ACROSS THE URALS AND THE BALTIC

We have attempted to determine to what extent, if at all, natural features such as the Urals and the Baltic affect Lg amplitudes. Because of the vertical absence of earthquakes providing source-receiver paths contained within Western Russia and the apparently similar Baltic shield regions, we have studied short-period recordings at WWSSN stations in Scandinavia from three nuclear explosions. These are situated to the west of the Urals (PNE shot on 4 October 1971), south of the Urals (Western Kazakh, 23 December 1969), and one east of the Urals (Eastern Kazakh, 30 November 1969). These events, their recording stations, and the source-receiver paths are shown in Fig. I-33. Epicentral distances range from 11° to 40°. Paths to UME, COP, and KON cross the Baltic; those to KEV and NUR do not. Lg was readily observed from these large explosions even up to 40° distance; its amplitude was generally quite small on the vertical component, and we have measured amplitudes on the horizontal-component recordings only. The largest peak-to-peak amplitude within 30 sec of the time corresponding to the 3.5-km/sec group velocity was measured. The Lg amplitude was in all cases not much smaller than that of P; its dominant period (1 to 2 sec) is unfortunately close to that of the prevailing noise.

Figure I-34 shows horizontal-component Lg amplitudes as a function of distance Δ, corrected for peak magnification and adjusted to $m_b = 6.0$ through

$$\text{Amplitude (6.0)} = \text{Amplitude} \times 10^{(6.0 - m_b)} \quad .$$

Note that these results seem to imply that, for an explosion of $m_b = 3.0$, the amplitude of Lg will be at least of amplitude 1 mμ at distances up to 30°. Short-period detection levels as small as 1 mμ have been claimed; thus, if Lg is of any use in a discrimination context it should be measurable for extremely small explosions across similar paths.

Amplitudes measured on the north-south component were always larger than those measured on the east-west component. The paths shown on Fig. I-33 run nearly in an east-west direction, and thus the maximum amplitude of Lg appears to be in the transverse component of motion, i.e., of Love-wave type.

For all the events studied, amplitudes at stations to the west of the Baltic are very close to those observed to the east. The Baltic, an extremely shallow sea within only a few isolated pockets of depths greater than 200 m, thus appears to have no observable effect upon the propagation of Lg.

Also shown on Fig. I-34 is a curve determined empirically by Nuttli[10] for the diminution of Lg amplitudes with distance in Eastern North America, given by

$$A(\Delta) = \kappa (\Delta \sin \Delta)^{-1/2} e^{-0.07 \Delta} \quad (I-1)$$

where Δ is distance in degrees, and κ is a constant, here set to 10^4. This appears to be a good fit to the data: note that the Lg amplitudes measured for the Eastern Kazakh event are quite consistent with Nuttli's relation. This may well indicate that the Urals have little effect upon Lg amplitudes.

Nuttli[10] has also derived an empirical relation between m_b and Lg amplitudes, given by

$$m_b = 1.66 \log \Delta + \log (A/T) \quad (I-2)$$

where A is the peak-to-peak amplitude in millimicrons of Lg, and T is its dominant period. Assuming T = 1 sec, Fig. I-35 shows m_b calculated from Lg as a function of distance. The

average m_b indicated is about 5.0, or one m_b less than that measured from teleseismic P-wave observations. In addition, Nuttli used Lg amplitudes measured from the vertical-component seismogram only, which, as we mentioned earlier, were considerably less than those observed on the horizontal components from which we measured A. It is thus possible that Lg amplitudes may be useful as a discriminant, if Eq. (I-2), determined for Eastern North America, is applicable to Western Russia.

<div style="text-align: right">R.G. North</div>

L. Pn, Sn, AND Lg AMPLITUDE-DISTANCE RELATIONSHIPS FOR EASTERN NORTH AMERICA

Amplitudes of the crustal phases Pn, Sn, and Lg for the Eastern North American events listed in Table I-10 were read from short-period, vertical-component seismograms of the Canadian seismograph network. As an aid in identification of the Pn phase, Massé's P-wave velocity model was used to calculate theoretical travel times. Calculations of theoretical Sn wave velocities assumed $V_p^2 = 3 V_s^2$.

Figures I-36 through I-38 present amplitude-distance plots normalized to $m_b = 3.6$ for the three phases. Though all show clear trends to amplitude decay with distance, Pn data are the most widely scattered for distances of less than 10°. Small events 6 and 8 with Pn magnitudes of 3.9 introduce this scatter. Examination of Fig. I-37 reveals that Sn amplitudes for these same events are mor densely clustered about the line of average decay than the Pn amplitudes of Fig. I-36. The   ter consistency of Sn readings is attributable to larger amplitudes (1.5 to 2 times Pn amplitude) at the same distances. These observations suggest that the scatter in

TABLE I-10						
EPICENTRAL DATA FOR EVENTS USED IN THIS STUDY						
Event	Date	Time	Latitude (°N)	Longitude (°W)	Magnitude	
					m_n	m_b
1. Baffin Island	4/24/73	03:55:04	71.7	71.2	4.7	4.2
2. Quebec-Maine	6/15/73	01:04:05	45.3	71.2	5.0	4.8
3. Blue Mountain Lake	7/15/73	08:20:31	44.0	74.4	3.4	–
Blue Mountain Lake	7/15/73	10:32:38	44.0	74.4	3.2	3.4
Mt. Wright, P.Q.[†]	1/12/74	15:58:02	52.7	67.6	3.5	–
5. Minnesota	7/09/75	14:54:15	45.6	96.0	–	4.6
6. Maniwaki, P.Q.	7/12/75	12:37:15	46.5	76.2	–	4.3
7. Western Quebec[‡]	8/21/75	21:42:51	48.1	78.0	3.6	–
8. Southwestern Quebec	12/19/75	15:25:11	47.0	78.8	3.8	–
9. Atlantic Ocean	10/06/75	22:21:41	49.6	57.0	–	5.2
† Mine blast						
‡ Rockburst in Malarctic Mine						

Pn amplitudes (for small events) may be due to comparatively low signal-to-noise ratios, and that magnitudes derived from Pn amplitudes for such events will be less useful in discrimination than magnitudes derived from the Sn and Lg phases.

The line of average decay for Pn amplitudes, shown in Fig. I-36, was found by Evernden.[11] A method similar to his yielded an average value for Sn decay with distance. The least-squares fit to a straight line was found for $\log_{10} (A/T)$ against $\log_{10}$ (distance) for each event with sufficient data. Six events combine to give an average value of -1.80, represented as a straight line in Fig. I-37. The same procedure gives an average value for Lg amplitude decay of -1.65. This number, the average of eight events, agrees closely with Nuttli's[10] value of -1.66. Figure I-38 shows a straight line with a slope of -1.66 as well as a curved line representing the theoretical attenuation of dispersed surface waves. The equation for this line is:

$$A = K(\Delta^{-1/3}) (\sin \Delta)^{-1/2} e^{-\gamma \Delta}$$

where A is the Airy phase amplitude, K is a constant, Δ is the distance in degrees, and γ is the coefficient of anelastic attenuation.[10]

Table I-11 lists the events used, the values of Sn and Lg amplitude decay with distance, and the standard deviations of the data points from the least-squares fit for each event. In Sec. M below, these amplitudes will be converted to magnitudes for a comparison between earthquake and explosion values.

<div align="right">

M. W. Shields
T. J. Fitch
R. E. Needham

</div>

TABLE I-11 AMPLITUDE FALLOFF WITH DISTANCE				
Event	Sn Slope	Standard Deviation	Lg Slope	Standard Deviation
6/15/73	−1.74	0.20	−1.31	0.17
7/15/73a	−	−	−1.58	0.07
7/15/73b	−	−	−1.52	0.15
1/12/74	−1.94	0.15	−1.93	0.12
7/09/75	−1.98	0.24	−1.84	0.26
7/12/75	−1.73	0.23	−1.48	0.15
8/21/75	−1.61	0.24	−2.01	0.17
12/19/75	−1.77	0.14	−1.55	0.26
Average	−1.80	0.20	−1.65	0.17

M. COMPARISON OF CRUSTAL-PHASE MAGNITUDES FOR EXPLOSIONS AND EARTHQUAKES

Magnitude relationships of the usual form

$$m = a + b \log \Delta + \log A/T \tag{I-3}$$

are used to test for systematic differences between explosions and shallow earthquakes recorded in the near-regional distance range from 5° to 20°. In the range the crustal phases Pn, Sn, and Lg are prominent of short-period seismograms. Magnitude formulas pertinent to Pn and Lg were taken from Evernden[11] and Nuttli,[10] respectively. The one for Sn was inferred from the amplitude-distance relationship determined empirically by Shields, Fitch, and Needham in Sec. L above. The study yielded -1.80 for the coefficient of the $\log \Delta$ term in Eq. (I-3). A value of 3.79 for the normalizing constant a in Eq. (I-3) was determined by equating teleseismic m_b to m_{Sn} for five earthquakes for which we have measured Sn amplitudes and periods. Figure I-39 represents a test of the Sn amplitude-distance relationship. The test is successful in that the magnitudes at individual stations scatter more or less uniformly about the mean Sn magnitude for the event regardless of the distance between source and receiver. The three magnitude relationships are as follows:

$$m_{Sn} = 3.79 + 1.80 \log \Delta + \log A/T$$

$$m_{Lg} = 3.30 + 1.66 \log \Delta + \log A/T \qquad \text{(Nuttli}^{10}\text{)}$$

$$m_{Pn} = 3.82 + 2.00 \log \Delta + \log A/T \qquad \text{(Evernden}^{11}\text{)}$$

where Δ is in degrees, and A/T is in microns/second.

Magnitudes were determined for one mine blast in Eastern Canada, four PNEs in Western Russia, the SALMON shot in Mississippi, and ten earthquakes located in Eastern North America. Amplitudes and periods were read from analog short-period records from LRSM, WWSSN, or the Canadian network. All magnitudes refer to maximum amplitudes of the vertical component of motion. The various magnitude estimates are listed in Table I-12. Figure I-40 shows that the ratio of Sn-to-Lg amplitude for explosions and earthquakes from this limited and possibly heterogeneous data set defines distinct populations in the distance range from 600 to 1300 km. Removing the distance dependence by converting amplitudes to magnitudes does not change the basic result. The m_{Lg} from explosions is about 0.3 of a magnitude unit less than m_{Lg}'s for earthquakes (Table I-12). Sn magnitudes for explosions and earthquakes are in close agreement with P-phase magnitudes, either m_{Pn} or m_b. Consequently, the magnitude ratio m_{Lg}/m_{Sn} will be distinct for these explosions and earthquakes as shown in Fig. I-41.

From these results a reasonable working hypothesis would be that explosions, either because of their shallow depth or the nature of the source, are comparatively poor exciters of Lg. Apparently, Sn excitation from explosions and earthquakes is comparable to P-wave excitation from these sources. For this to be so, the Sn from explosions must be primarily a P-to-S reflection at the free surface near the source. Furthermore, the efficient propagation of Sn or Pn, and their respective apparent velocities, implies that these phases are trapped in the lithosphere, as would be the case for wide-angle reflections. This model for Sn and Pn propagation is also consistent with the amplitude-distance plots for these phases shown in Sec. L above. Pn amplitudes show no pronounced distance dependence, whereas Sn amplitudes do. Apparently, the

TABLE 1-12
MAGNITUDE ESTIMATES FOR EARTHQUAKES AND EXPLOSIONS

Earthquakes

Event	m_b (Sn)	m_b (Pn)	m_b (ISC)	Mn
4/24/73	4.5 (7)[a]	4.7 (3)	4.2	4.8 (7)
6/15/73	5.0 (6)	4.9 (5)	4.8	4.9 (6)
7/15/73	3.2 (3)	3.2 (1)	–	3.4 (ISC)
7/15/73	–	–	3.4	3.2
11/30/73	4.3 (3)	4.5 (1)	–	4.5 (6)
7/09/75	4.6 (6)	4.4 (6)	4.6	4.8 (7)
7/12/75	4.3 (8)	3.7 (6)	4.3	4.2 (8)
8/21/75	3.7 (4)	3.8 (2)	–	3.6 (5)
10/06/75	5.2 (7)	5.3 (7)	5.2	–
12/19/75	3.8 (4)	3.9 (3)	–	3.8 (4)

Explosions

Event	m_b (Sn)	m_b (Pn)	m_b (ISC)	Mn
10/22/64[b]	4.4 (5)	4.3 (23)	4.4[c]	4.0 (10)
1/12/74[d]	3.9 (7)	–	–	3.5 (7
7/10/71[e]	4.7 (3)	4.8 (3)	5.2	4.2 (3)
9/19/71	4.1 (2)	4.5 (4)	4.5	3.7 (3)
10/04/71	4.4 (3)	5.0 (3)	4.6	3.9 (3)
9/04/72	4.4 (3)	4.3 (4)	4.6	4.2 (3)

a. Numbers in parentheses are those of amplitude readings.

b. SALMON nuclear test.

c. From Jordan et al.[12]

d. Western Quebec mine blast.

e. All following explosions were located in Western Russia.

signal-to-noise ratio for the Pn signals is significantly lower than that for the Sn signals. This disparity can be explained in terms of the wide-angle reflection hypothesis. Pn energy, having the higher phase velocity, tends to leak energy out of the lithosphere, whereas Sn energy tends to be trapped. Of course, scattering and anelastic attenuation will contribute to amplitude diminution of both phases. This speculation should be tested with more observations and by comparisons of real and synthetic seismograms.

<div align="right">

T. J. Fitch
M. W. Shields
R. E. Needham

</div>

REFERENCES

1. Seismic Discrimination SATS, Lincoln Laboratory, M.I.T. (30 September 1977), p. 44, DDC AD-A050584.

2. A. Ryall, "Seismic Identification at Short Distances," Proc. Woods Hole Conf. on Seismic Discrimination, Geotech Corp., Alexandria, VA (1970).

3. R. P. Massé, "Compressional Velocity Distribution Beneath Central and Eastern North America," Bull. Seismol. Soc. Am. 63, 911-935 (1973).

4. R. P. Massé and S. S. Alexander, "Compressional Velocity Distribution Beneath Scandinavia and Western Russia," Geophys. J. R. Astr. Soc. 39, 587-602 (1974).

5. Seismic Discrimination SATS, Lincoln Laboratory, M.I.T. (30 September 1977), pp. 63-67, DDC AD-A050584.

6. S. S. Alexander, "Long-period Seismic Methods for Identifying Small, Underground Nuclear Explosions," Final Report AFOSR Project 69-1796, Pennsylvania State University, University Park, PA (1973).

7. F. Press, G. Deward, and R. Gilman, "A Study of Several Diagnostic Techniques for Identifying Earthquakes," J. Geophys. Res. 68, 2909-2928 (1963).

8. M. Bath, Introduction to Seismology (Wiley, New York, 1973), pp. 325-326.

9. W. M. Ewing, W. S. Jardetzky, and F. Press, Elastic Waves in Layered Media (McGraw-Hill, New York, 1957), pp. 219-222.

10. O. W. Nuttli, "Seismic Wave Attenuation and Magnitude Relations for Eastern North America," J. Geophys. Res. 78, 876-885 (1973).

11. J. F. Evernden, "Magnitude Determination at Regional and Near-Regional Distances in the United States," Bull. Seismol. Soc. Am. 57, 591-639 (1967).

12. J. N. Jordan, W. V. Mickey, W. Helterbran, and D. M. Clark, "Travel Times and Amplitudes from the Salmon Explosion," J. Geophys. Res. 71, 3469-3482 (1966).
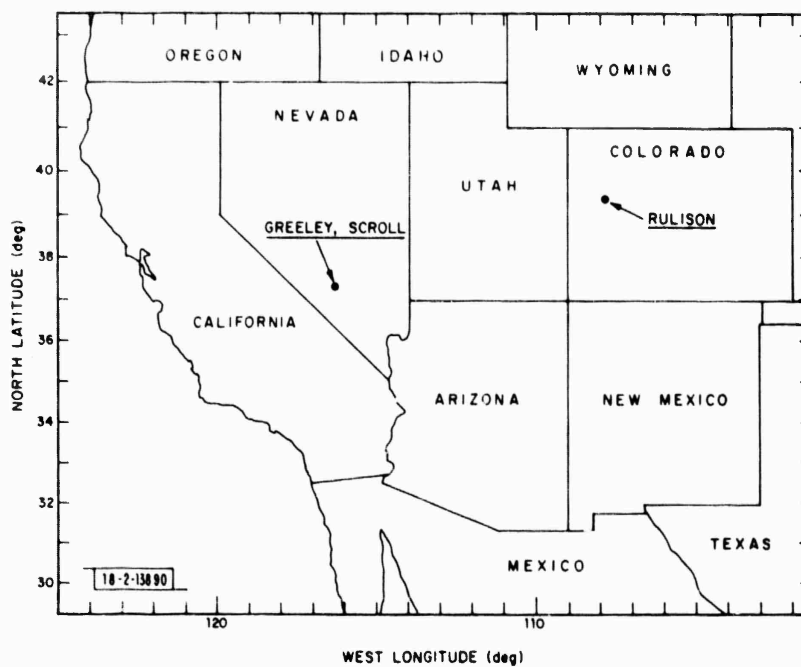
Fig. I-1. Event epicenters for Western U.S. explosions.

22
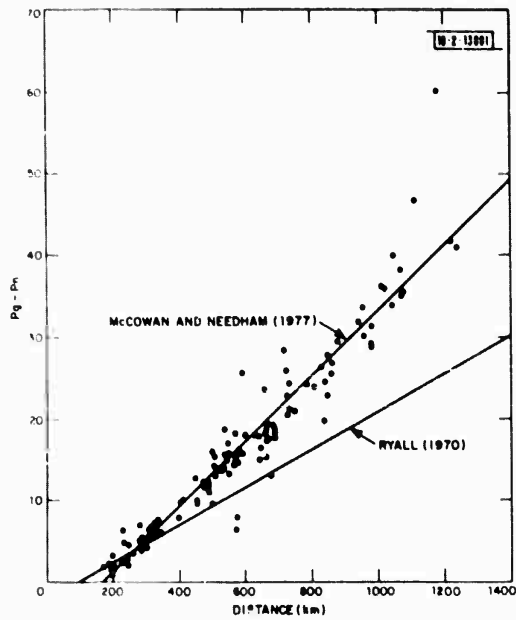
Fig. I-2. Pg – Pn travel-time differences
for NTS explosions.
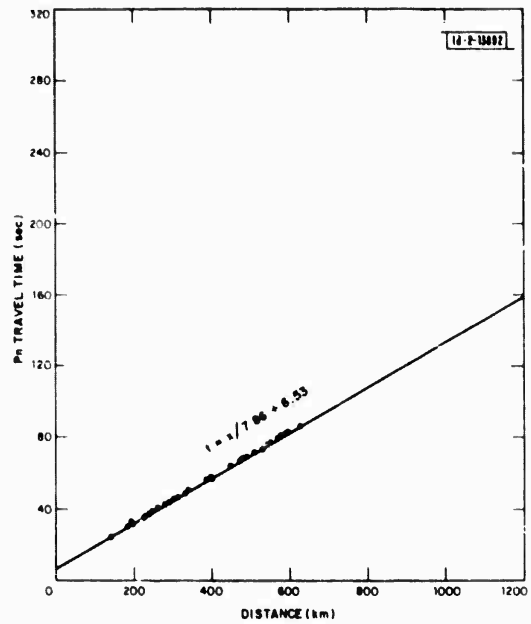
Fig. I-3. Pn travel times for NTS
explosions and best-fitting model
(72 observations).
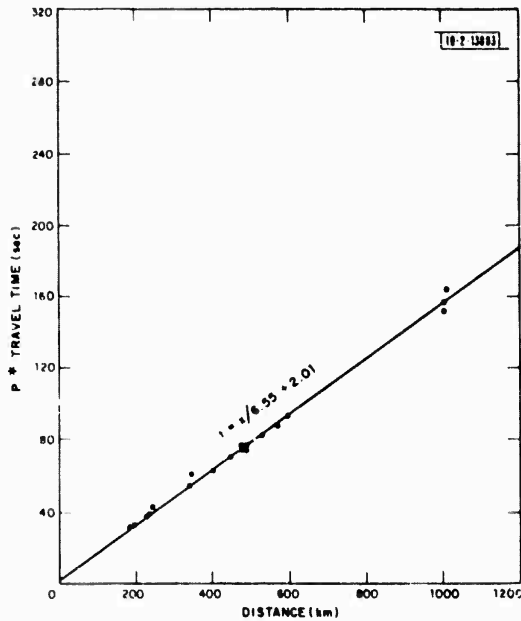
Fig. I-4. P* travel times for NTS
explosions and best-fitting model
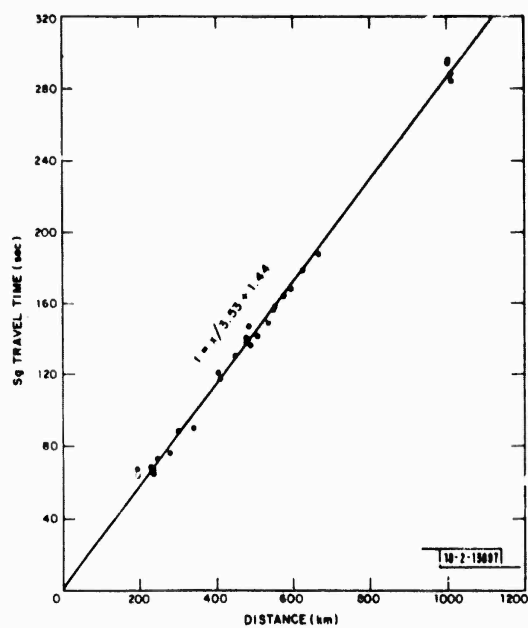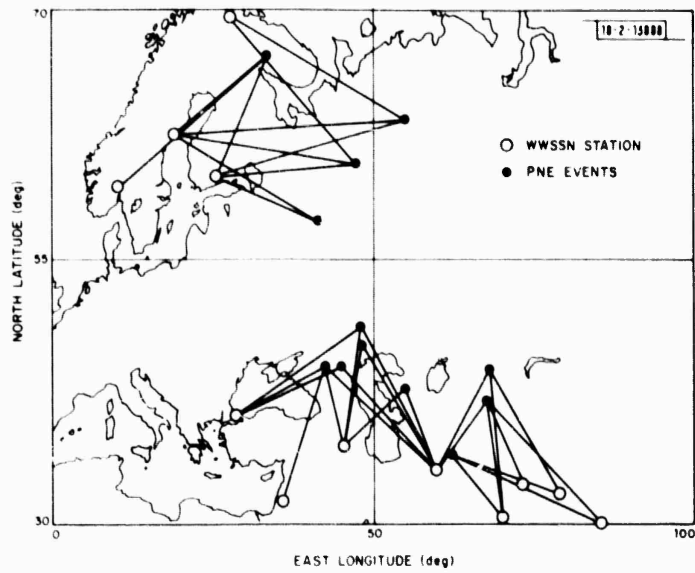(20 observations).
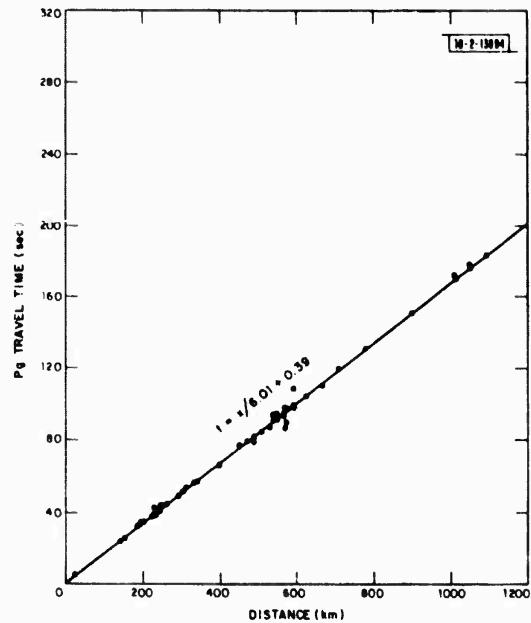
Fig. I-5. Pg travel times for NTS
explosions and best-fitting model
(74 observations).

23
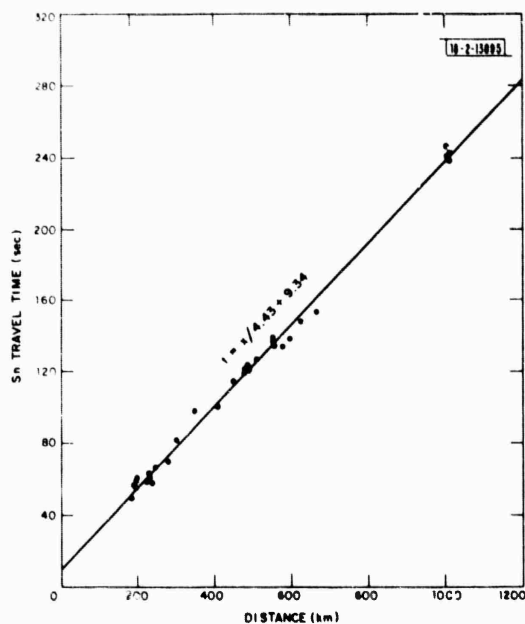
Fig. I-6. Sn travel times for NTS
explosions and best-fitting model
(39 observations).
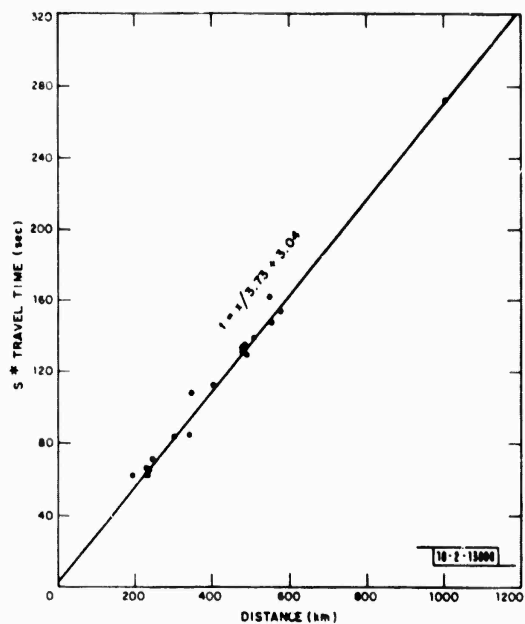
Fig. I-7. S* travel times for NTS
explosions and best-fitting model
(23 observations).

Fig. I-8. Sg travel times for NTS
explosions and best-fitting model
(32 observations).

24

Fig. I-9. Source-receiver paths used in this study.
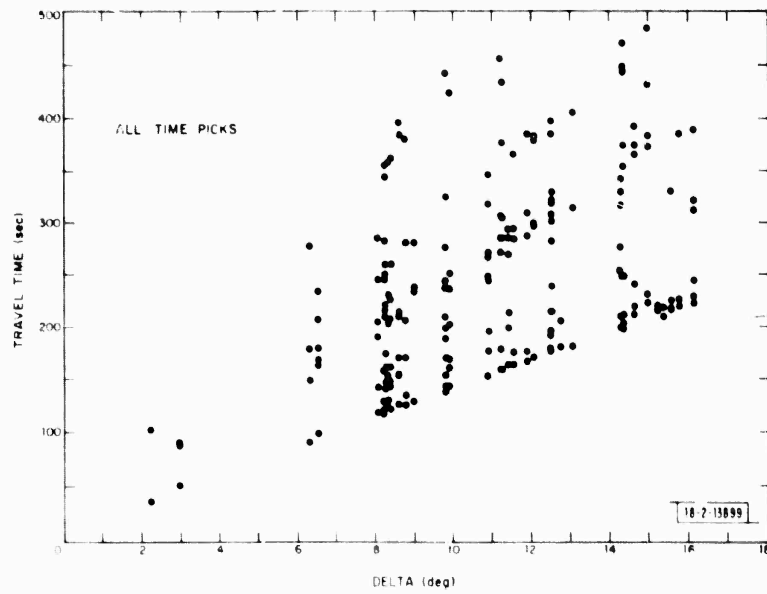
Fig. I-10. Analyst time picks made from 35 seismograms.
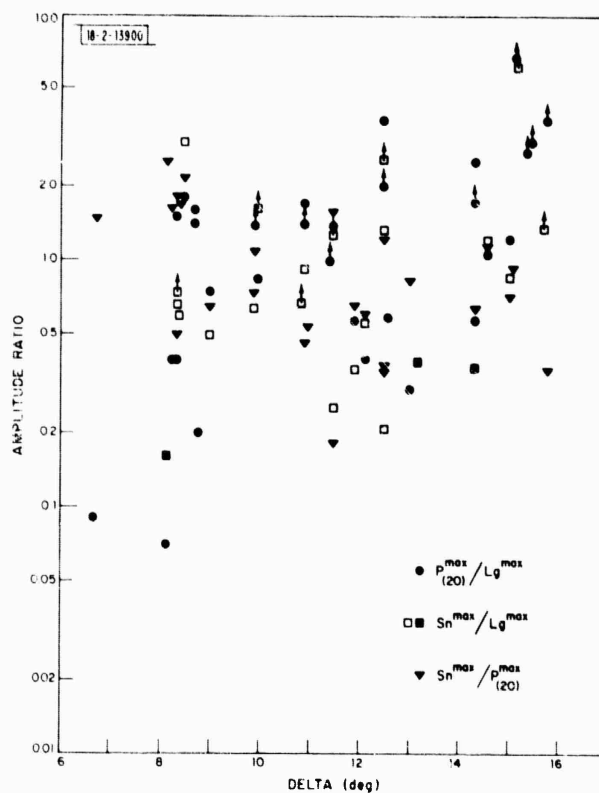
Fig.I-11. Amplitude ratios of (Pn/Sn), (Pn/Lg), and (Sn/Lg) measured from seismograms as a function of distance.
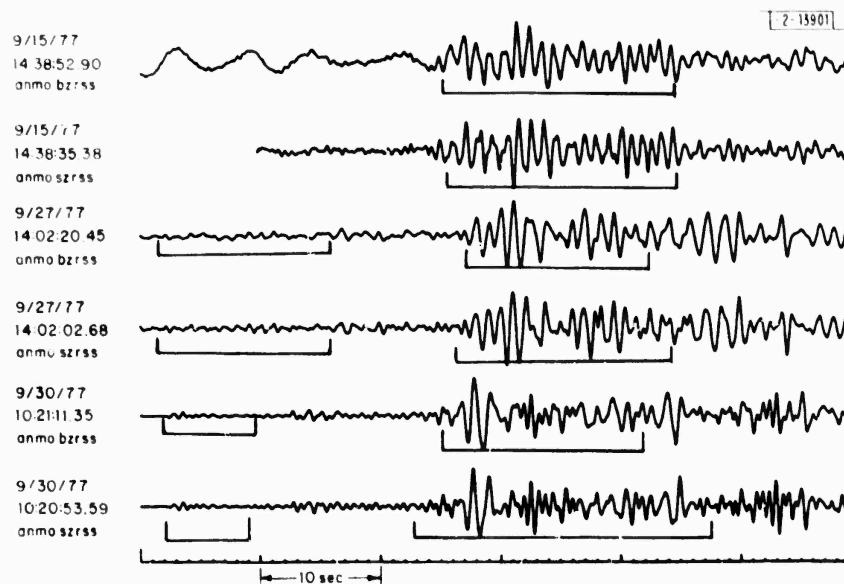
Fig. I-12(a). Broad-band and short-period SRO recordings of Pn and Pg.
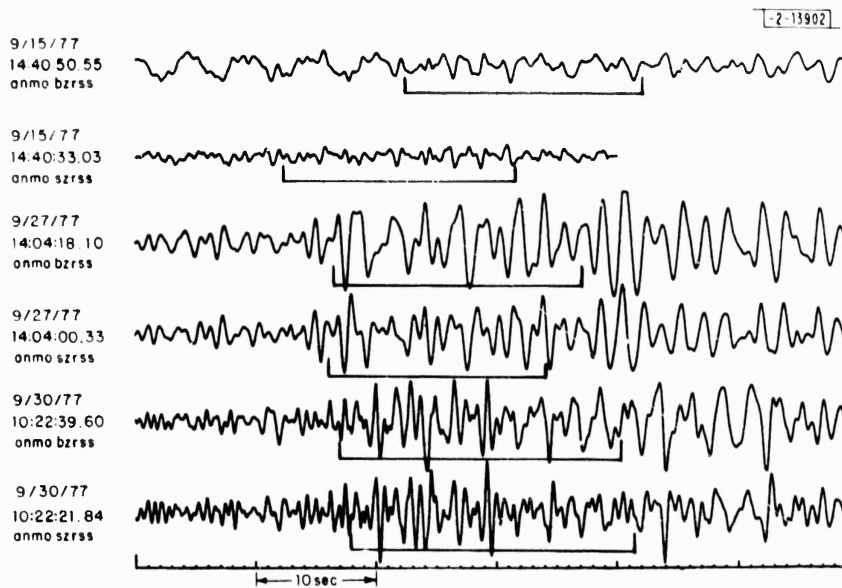
Fig. I-12(b). Broad-band and short-period SRO recordings of Lg.
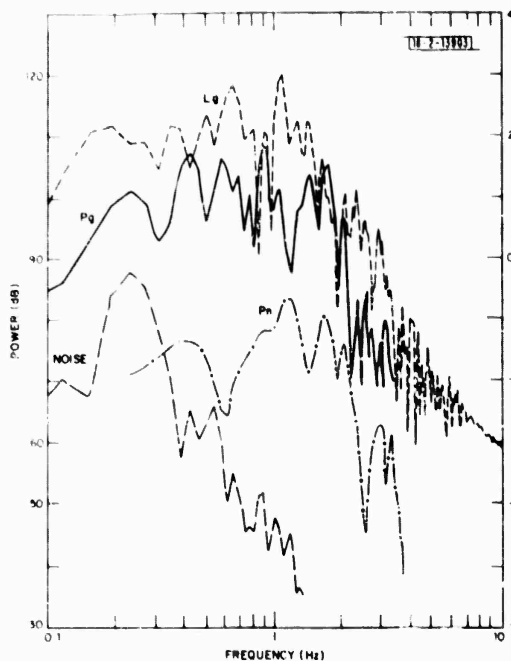
Fig. I-13(a). Utah earthquake,
30 September 1977, vertical
broad-band SRO at ALQ.
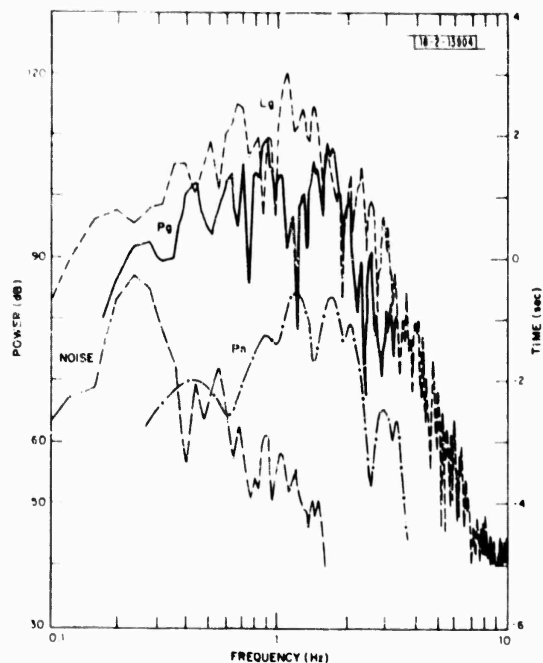
Fig. I-13(b). Utah earthquake,
30 September 1977, SP-Z SRO
at ALQ.
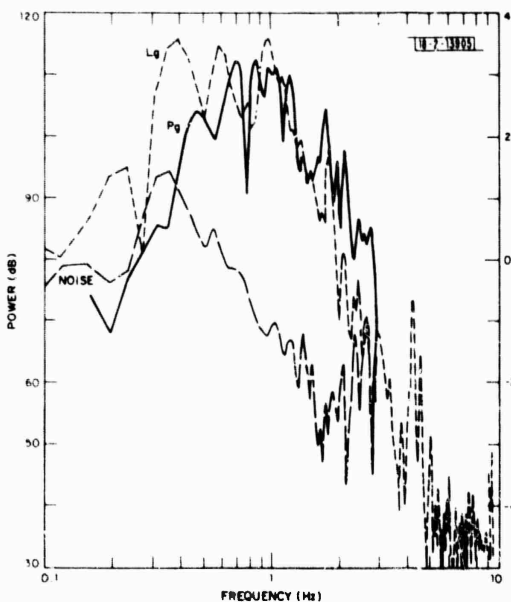
Fig. I-14(a). NTS, 27 September 1977,
SP-Z SRO at ALQ.
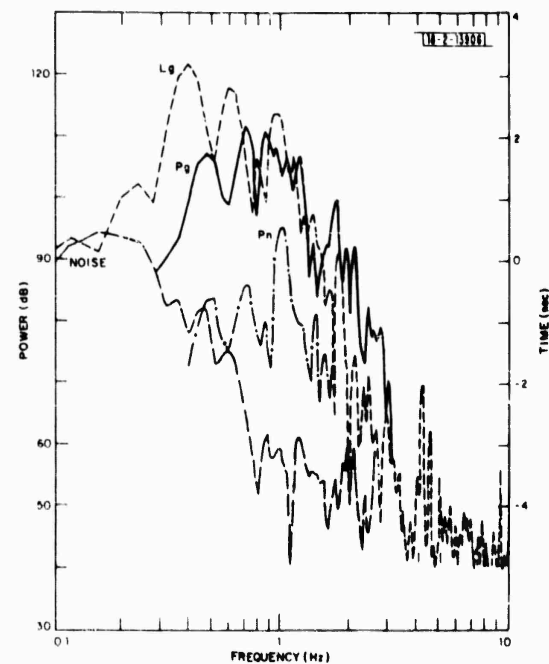
Fig. I-14(b). NTS, 27 September 1977,
vertical broad-band SRO at ALQ.

28
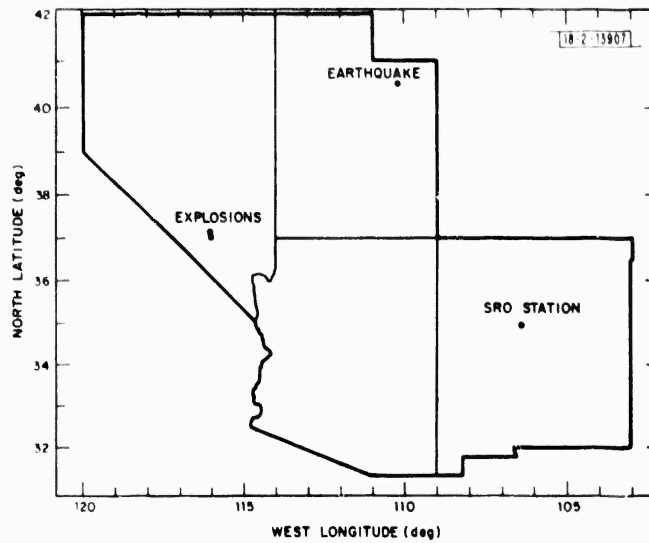
Fig. I-15. Distribution of events.
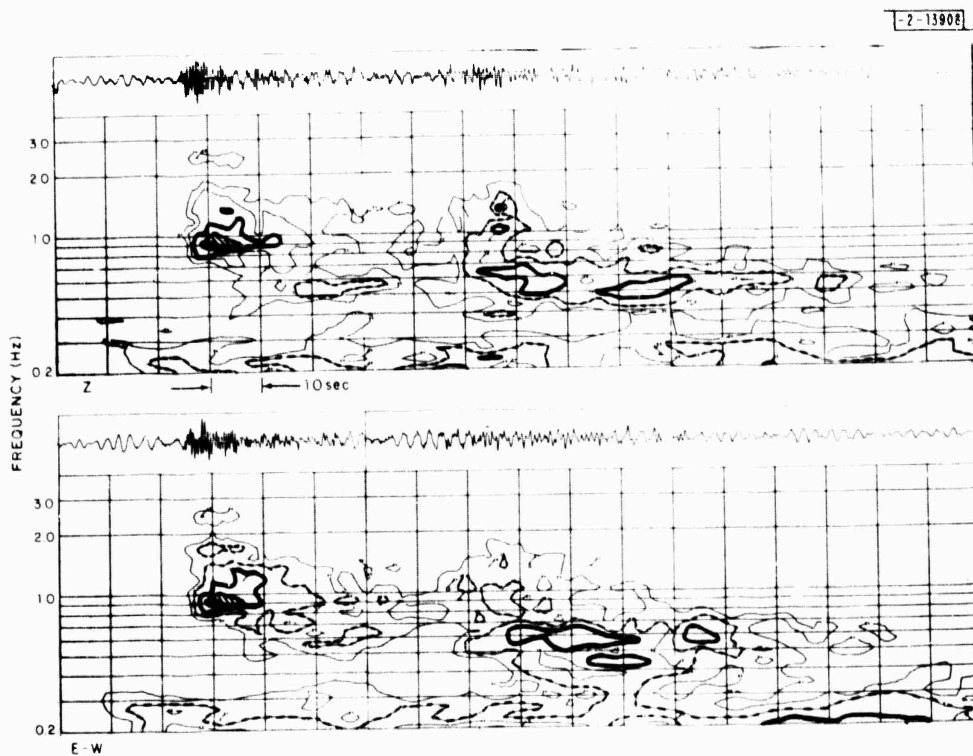
Fig. I-16. Sonograms of ANMO broad-band recordings of NTS event m_b 3.5.
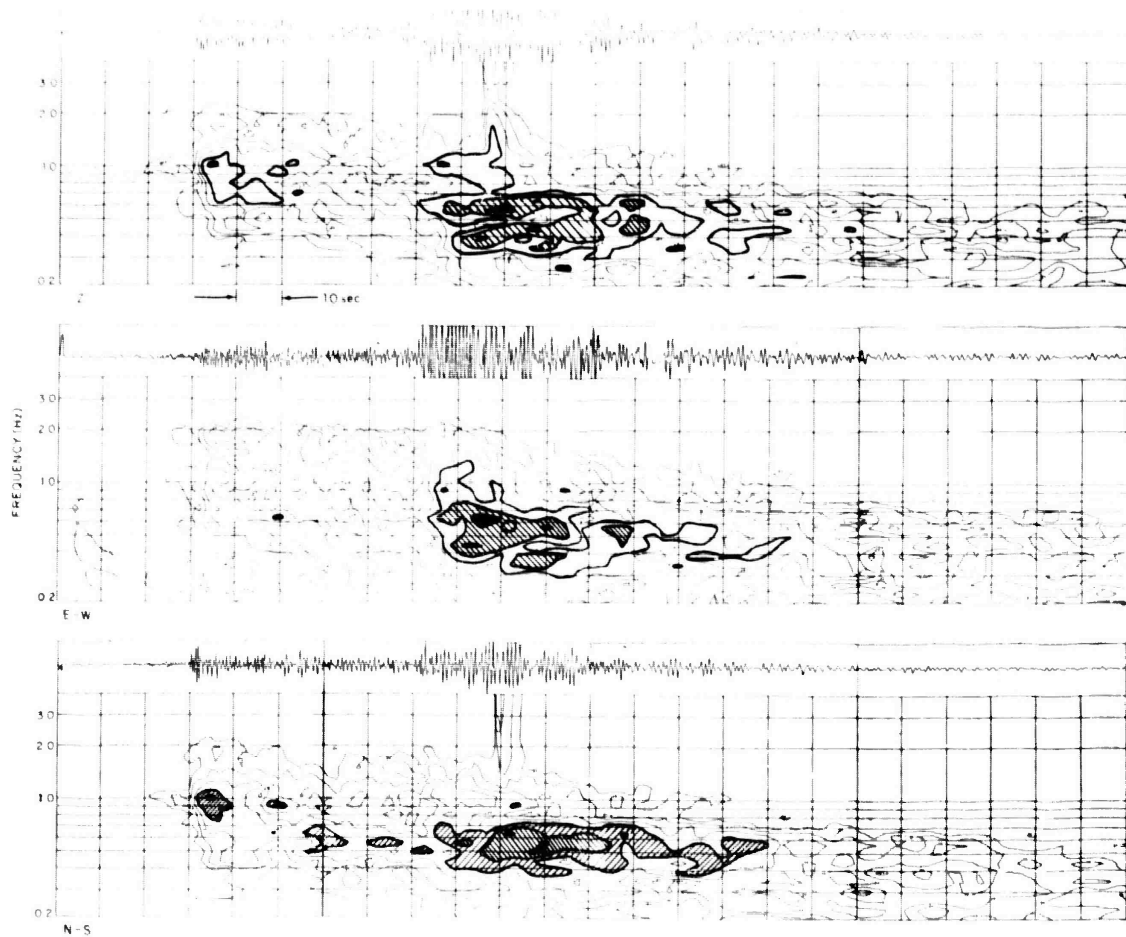
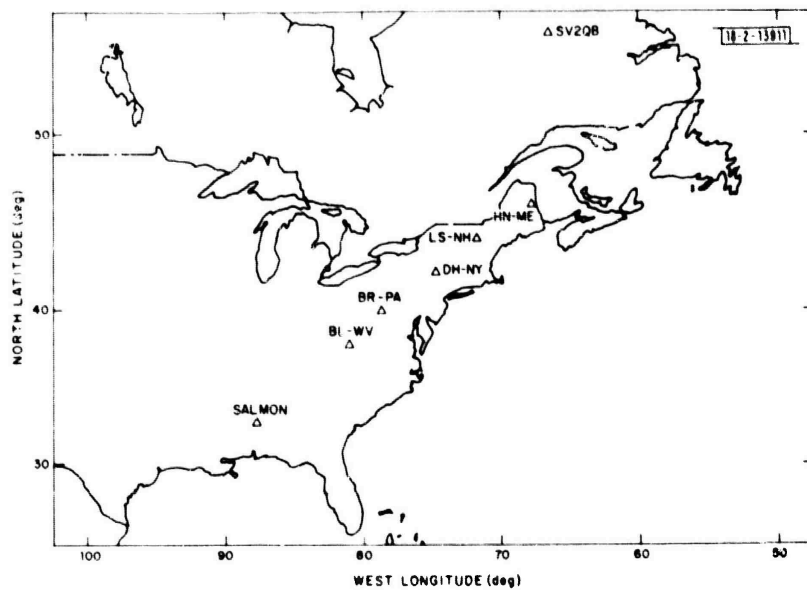Fig. I-17. Sonograms of ANMO broad-band recordings of NTS event m_b 5.0.
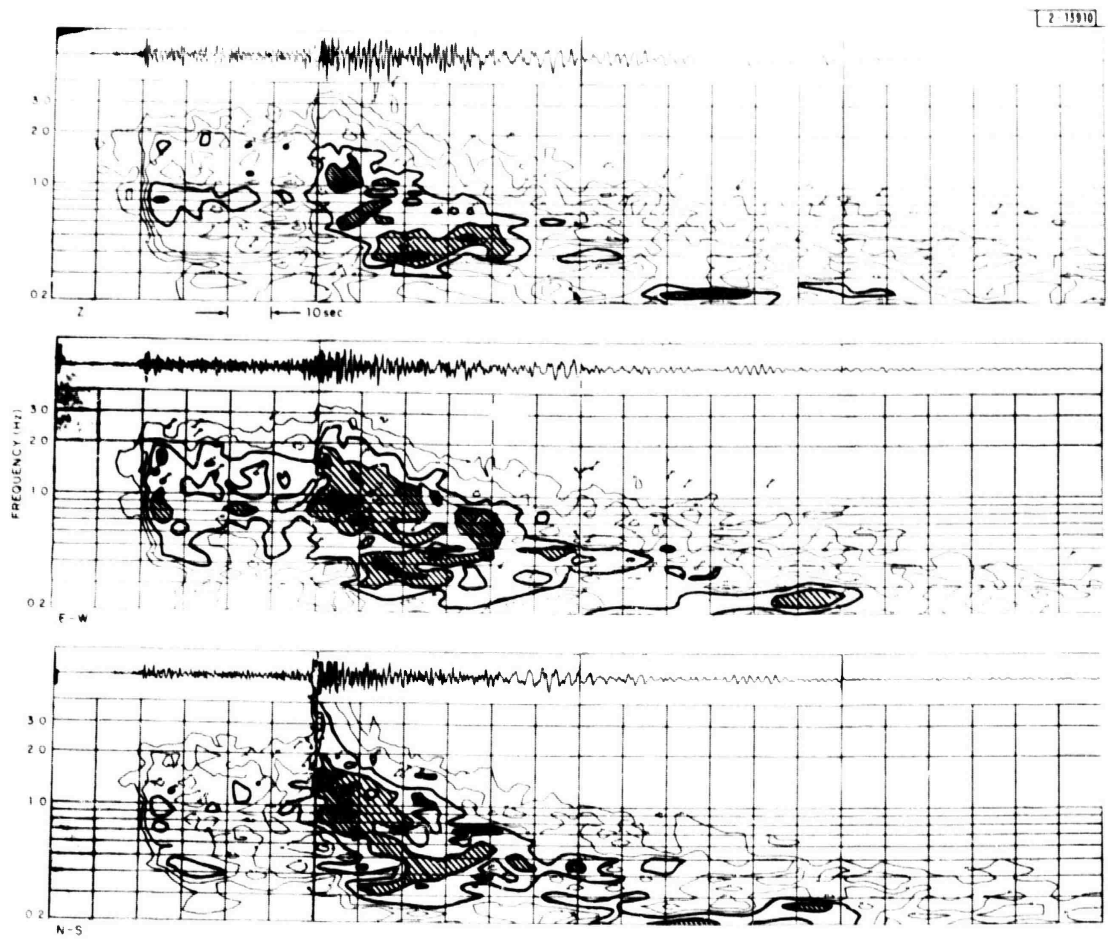
Fig. I-18. Sonograms of ANMO broad-band recording
of Utah earthquake m_b 5.0.
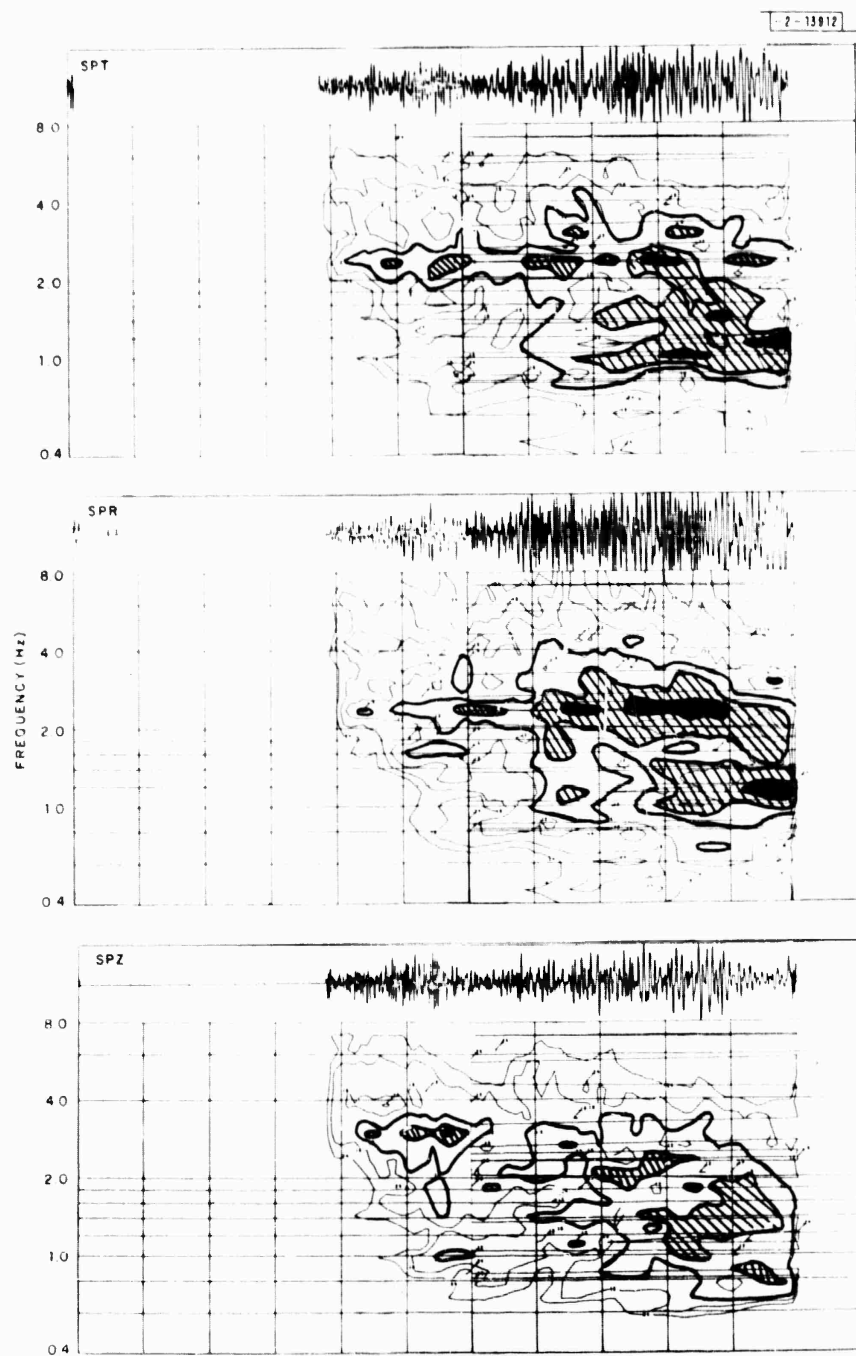
Fig. I-19. East coast LRSM stations for SALMON.

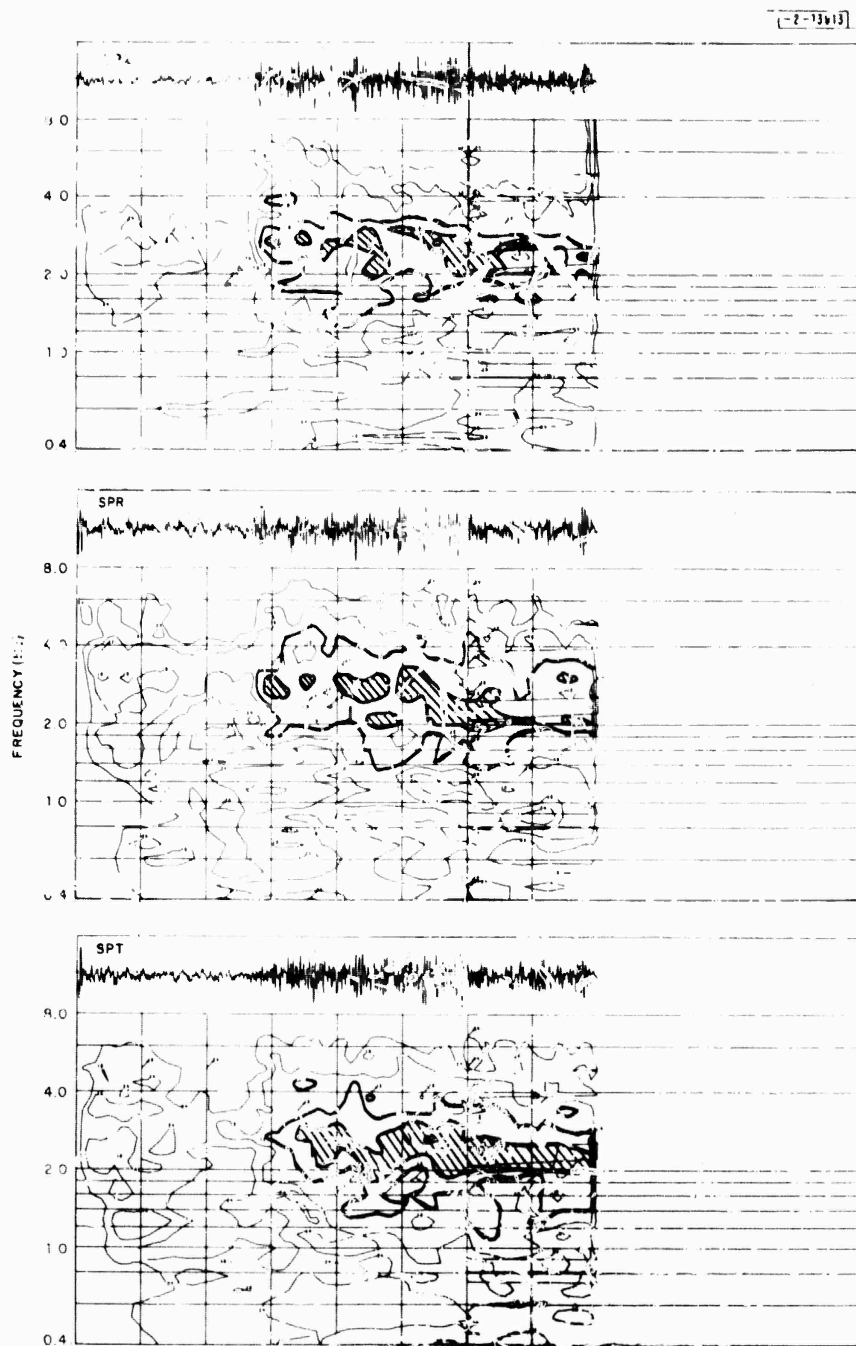Fig. 1-20. SALMON sonograms, station EU-AL.

33

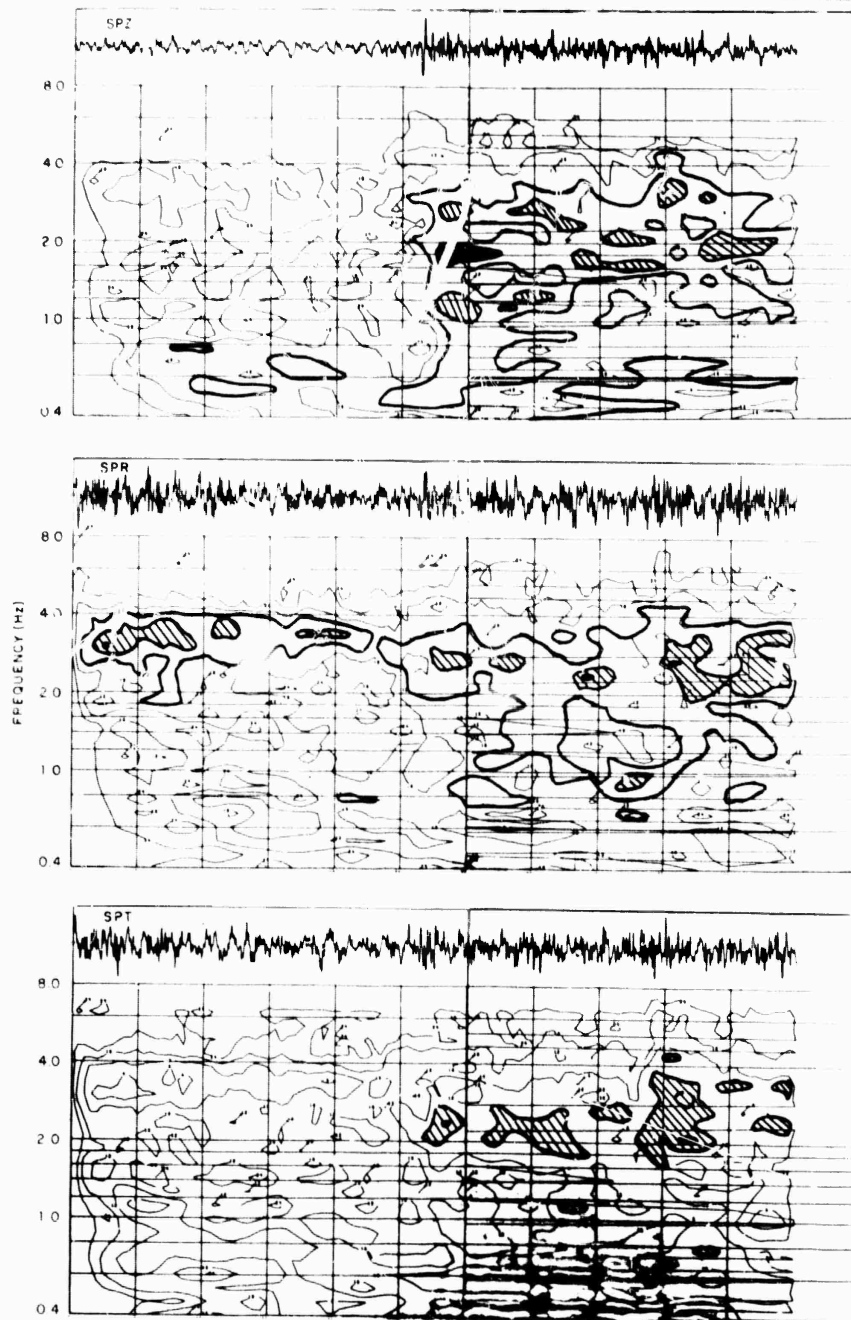Fig. I-21. SALMON sonograms, station BR-PA.

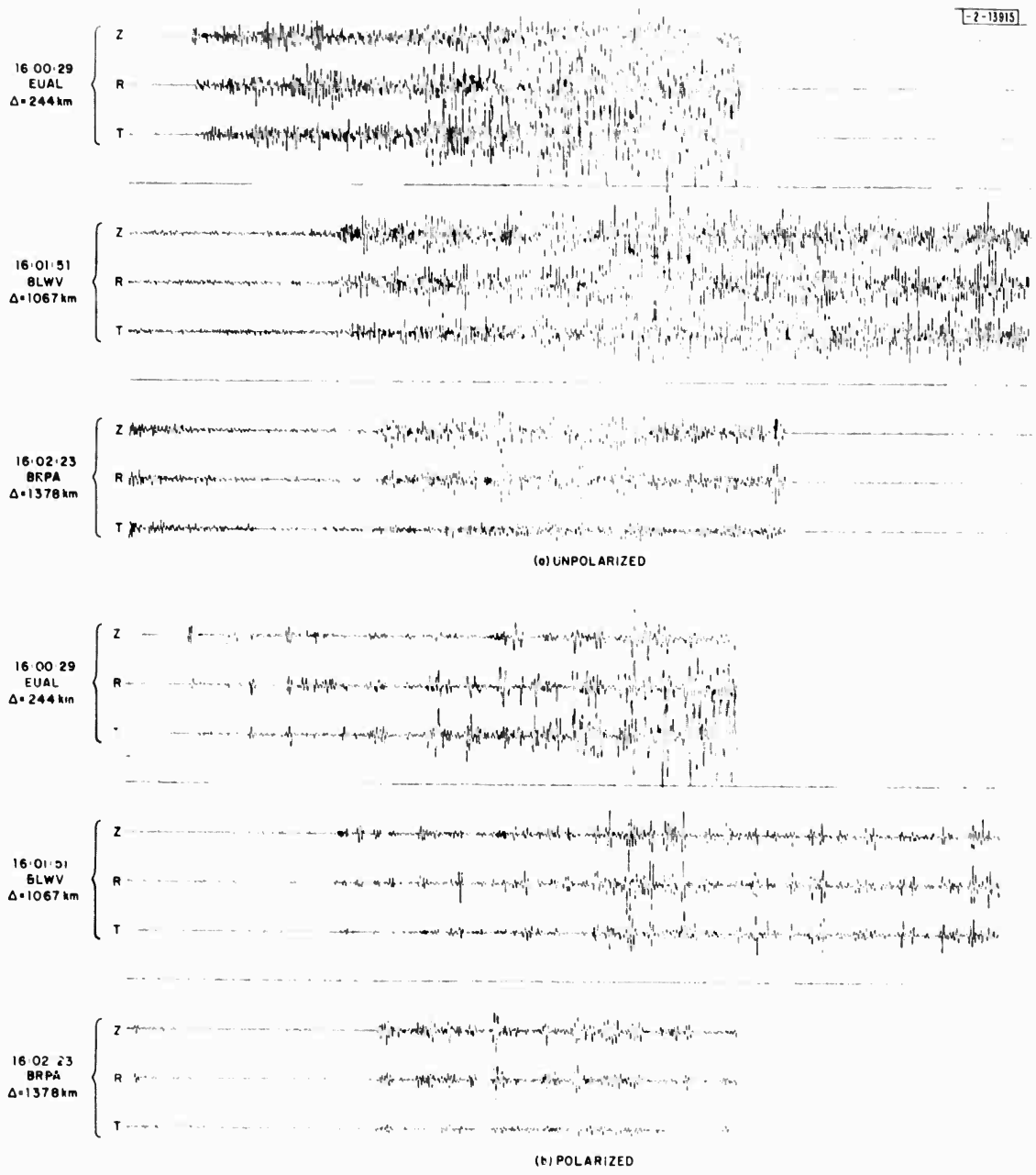Fig. I-22. SALMON sonograms, station DH-NY.

Fig. I-23. (a) Rotated 3-component data from SALMON recorded at LRSM stations EU-AL, BL-WV, and BR-PA. (b) Polarized data as described in text with cutoff ellipticity ϵ_0 = 0.25 and filter order n = 3.
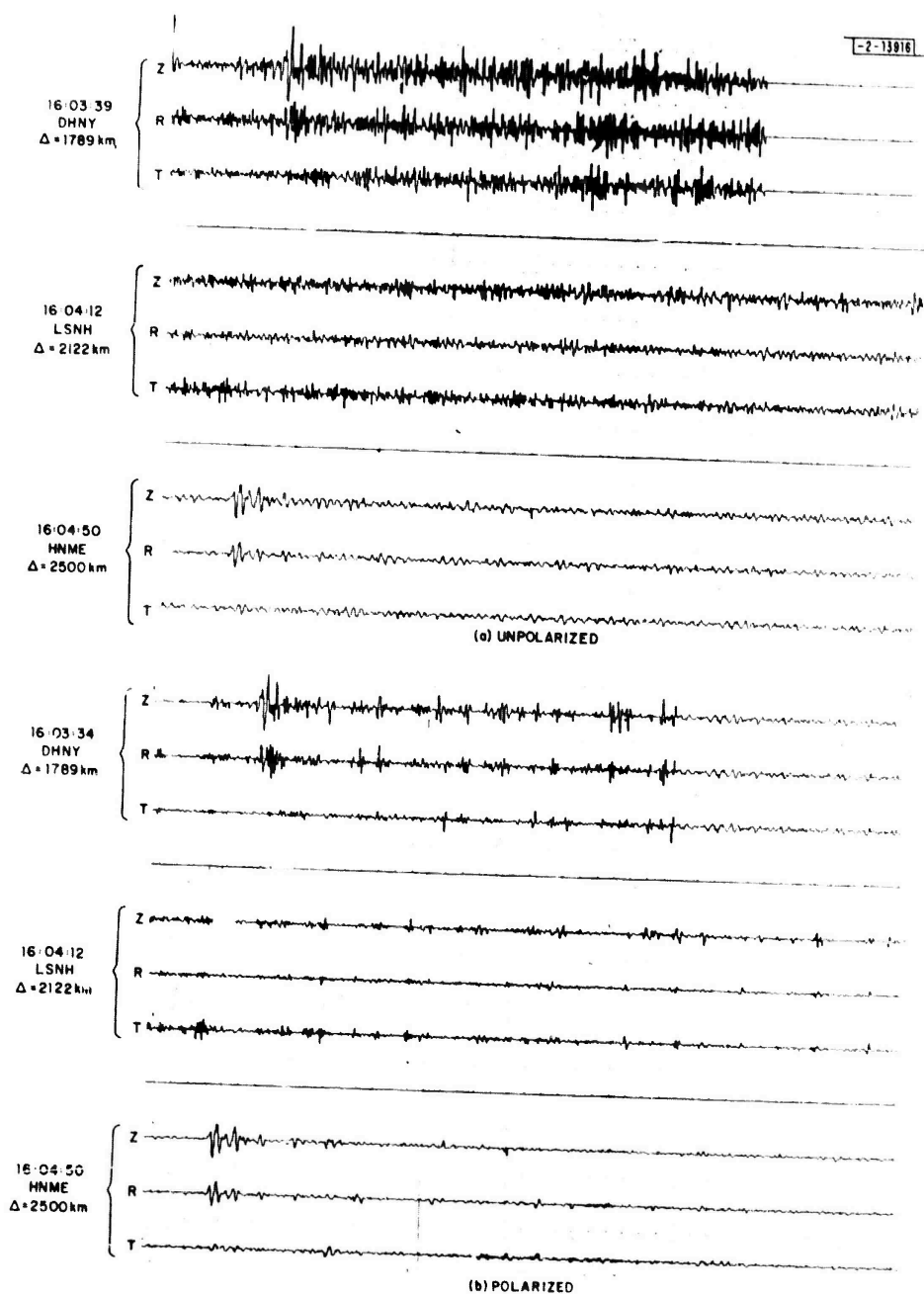
36

Fig. I-24. (a) Rotated 3-component data from SALMON recorded at LRSM stations DH-NY, LS-NH, and HN-ME. (b) Polarized data with cutoff ellipticity $\epsilon_o = 0.25$ and filter order $n = 3$.
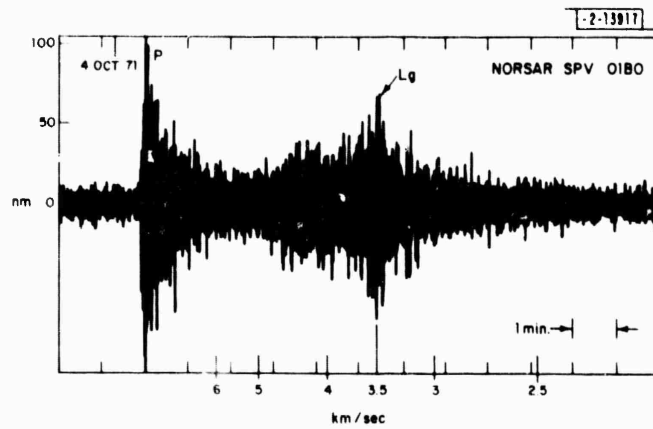
37

Fig. I-25. Short-period vertical NORSAR recording of event in Western Russia with Δ = 17.3° and back azimuth 65°.
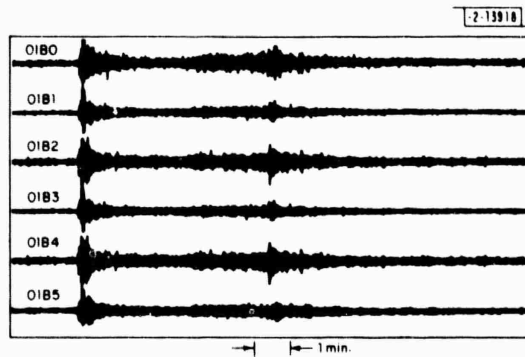

Fig. I-26. NORSAR subarray 1B data for event in Fig. I-25.

Fig. I-27. Wavenumber spectrum at 1.2 Hz of initial P-wave arrival (K = frequency/phase velocity). Peak in due east direction is primarily due to aliasing of P-wave peak.
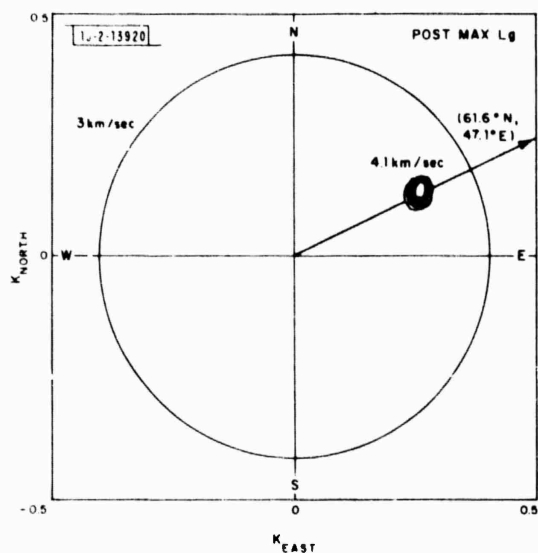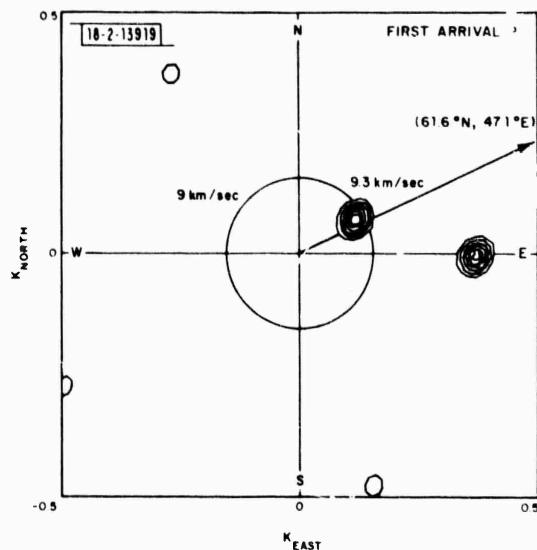
Fig. I-28. Wavenumber spectrum at 1.2 Hz of section immediately following maximum Lg amplitude (K = frequency/phase velocity).

39
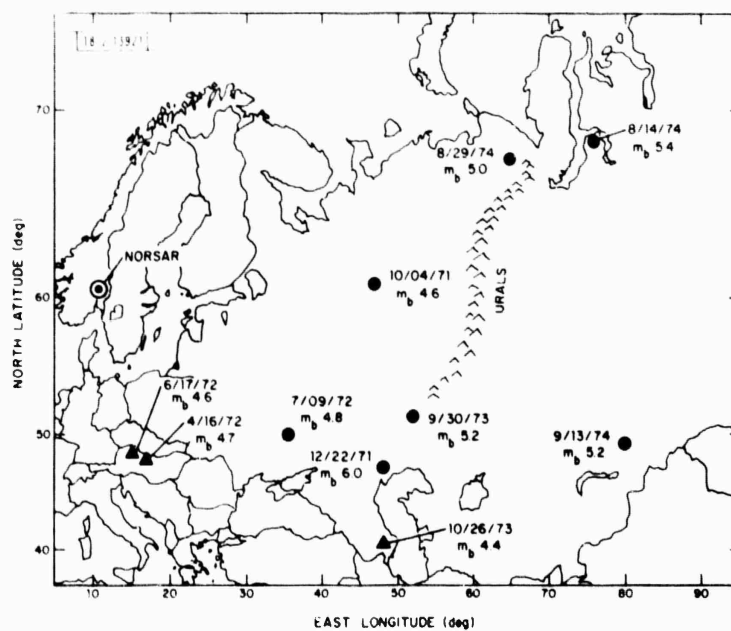
Fig. I-29. Map showing epicenters of presumed explosions in Western Russia and three earthquakes recorded at NORSAR. These events have sufficiently long recorded codas to include Lg arrivals on Sp vertical sensors.
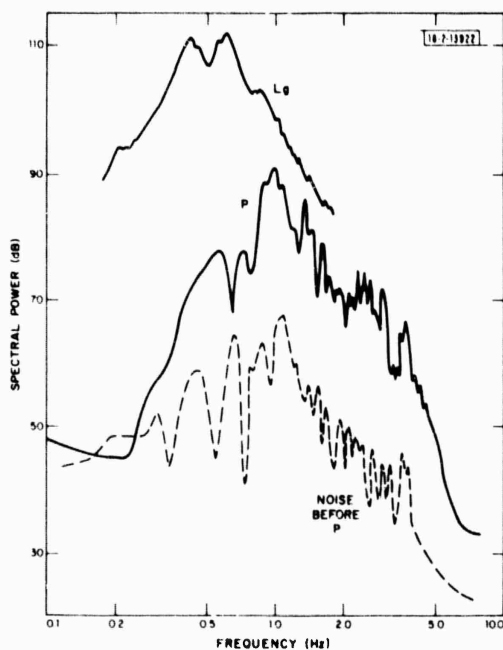
Fig. I-30. Spectra of 20-sec windows of P, Lg, and noise before P of event 3 — Austrian earthquake of 16 April 1972. Note that signal/noise ratio of P phase is nearly 20 dB from 1 to 4 Hz. m_b = 4.7, Δ = 13.5°.

Fig.1-31. Spectra of 20-sec windows of P, Lg, and noise before P of event 5 — PNE of 9 July 1972. Note higher frequency character of P wave and lower level of Lg spectrum compared with Fig.1-30. m_b = 4.8, Δ = 17.7°.
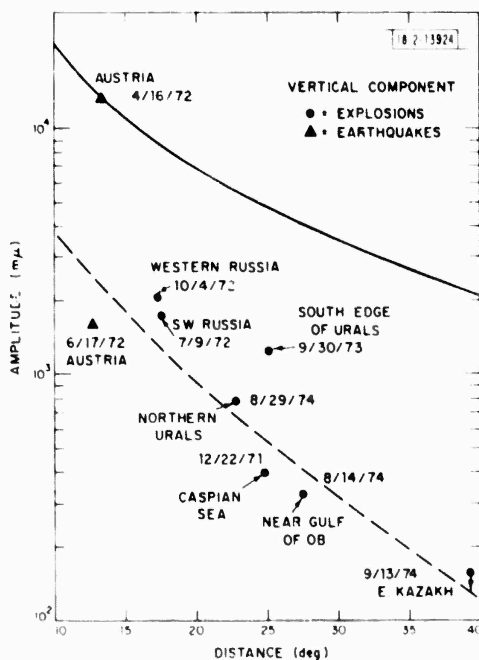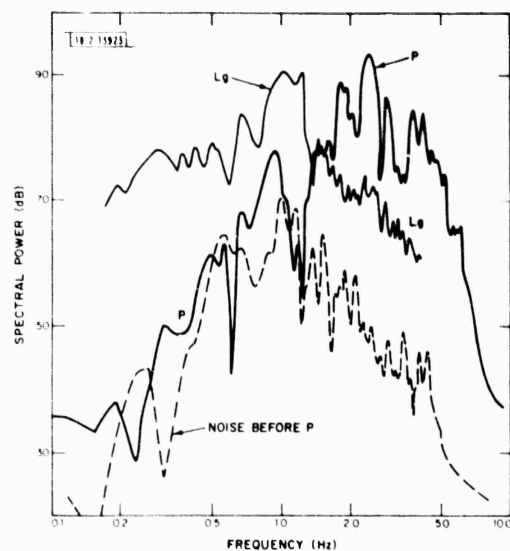

Fig.1-32. NORSAR measurements of Lg amplitudes normalized to m_b 6.0. This was done for each event by scaling Lg amplitude by factor 10^{6-m_b}. Dashed curve is Nuttli's theoretical trend of Lg amplitude vs distance for earthquakes in Eastern U.S., shifted here to pass through data. Solid curve is Nuttli's empirical variation of Lg with distance for m_b 6.0 earthquakes based on a short-period, surface-wave magnitude scale.

41
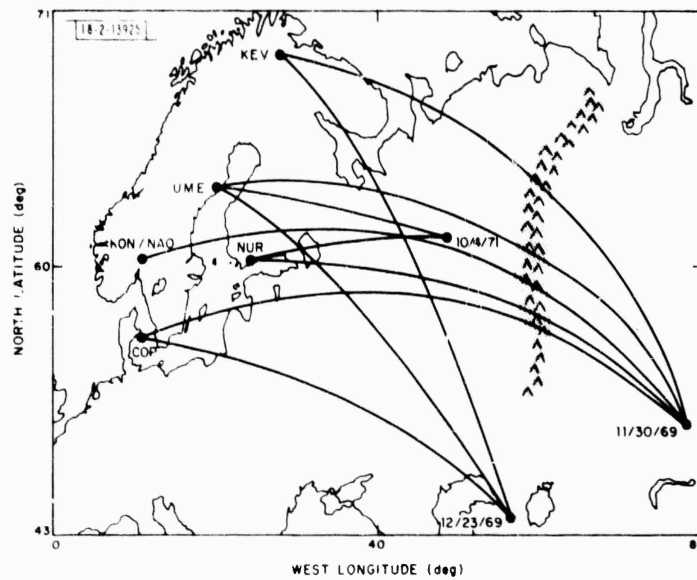
Fig. I-33. Source-receiver paths used in this study. Urals are indicated by shaded region.
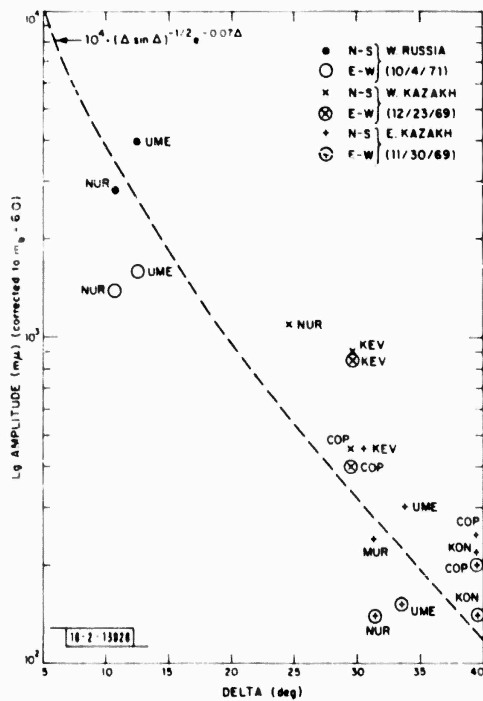
Fig. I-34. Lg amplitudes, separated into measurements from short-period north-south and east-west component seismograms. Also shown is Nuttli's[10] relation for amplitude dimension of Lg, with $\kappa = 10^4$.
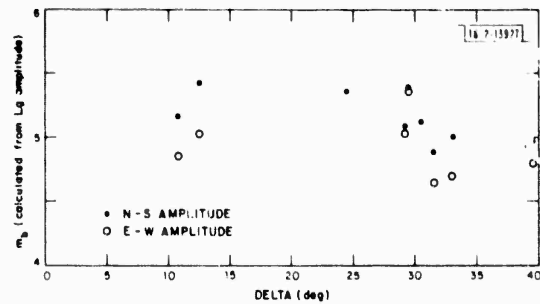
Fig. I-35. m_b calculated from Lg using Nuttli's[10] relation.
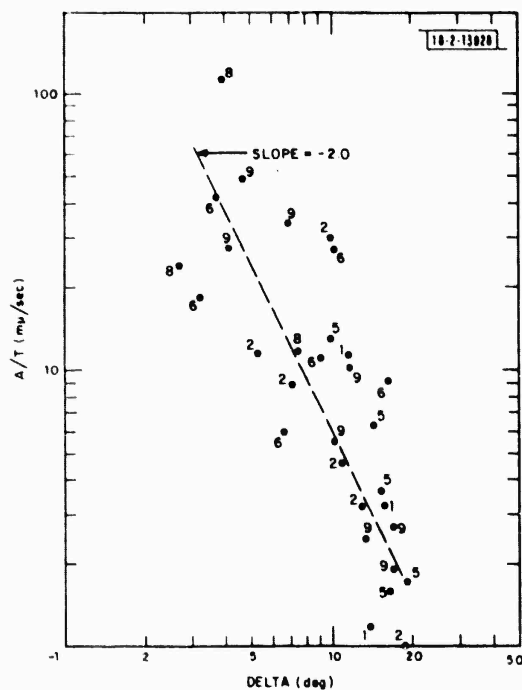
Fig. I-36. Pn amplitude vs distance.
Numbers correspond to event numbers
in Table I-10. Slope of line of average
decay is −2.0.
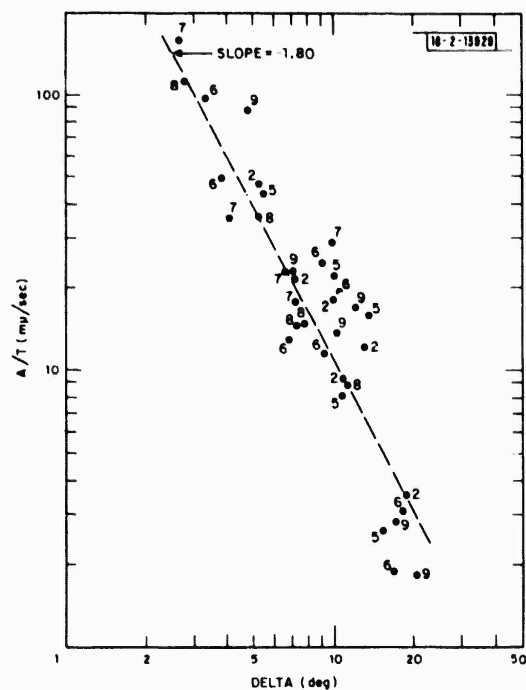
Fig. I-37. Sn amplitude vs distance.
Numbers correspond to event numbers
in Table I-10. Slope of line is −1.80.
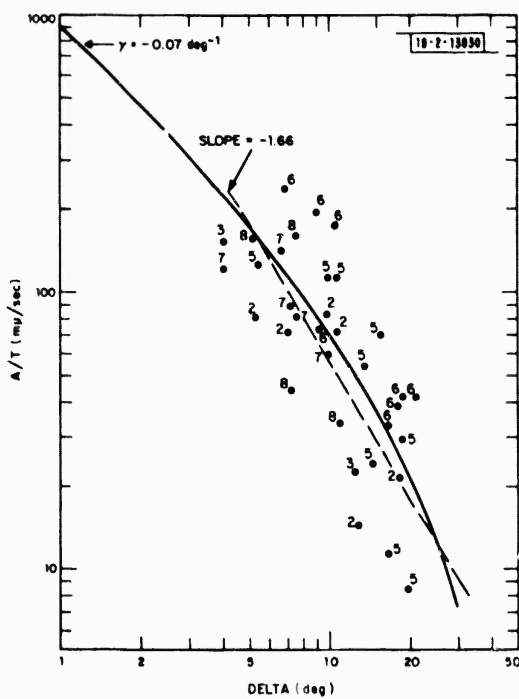
Fig. I-38. Lg amplitude vs distance.
Slope of straight line is −1.66. Co-
efficient of anelastic attenuation for
theoretical curve is γ = 0.07 deg^{-1}.
Numbers correspond to event num-
bers in Table I-10.

3
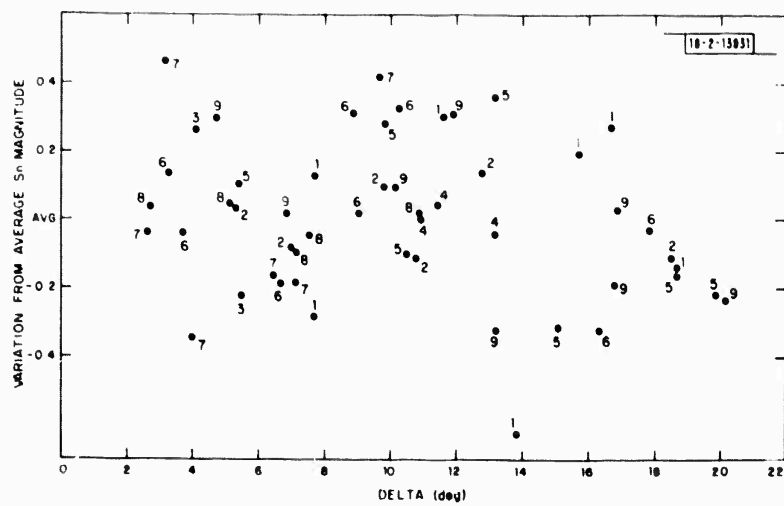
Fig. 1-39. Sn magnitude vs distance.
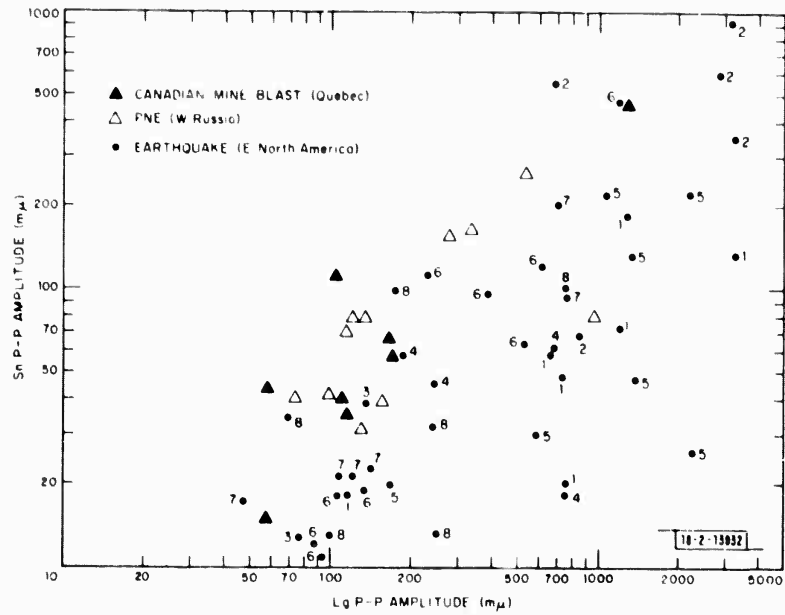
Fig. I-40. Sn vs Lg amplitudes.

Fig. I-41. Sn vs Lg magnitudes.
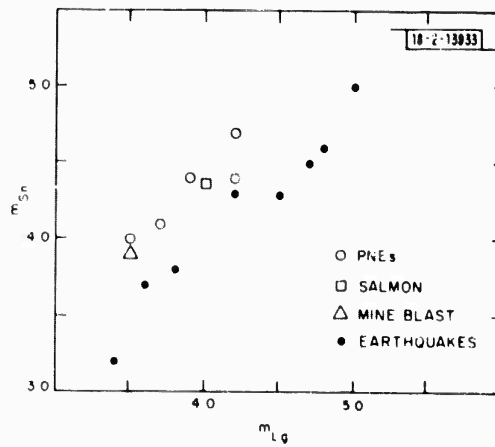
II. MISCELLANEOUS STUDIES

A. OCEAN-BOTTOM SEISMOMETERS FOR NUCLEAR MONITORING AND RESEARCH: A REASSESSMENT

Ocean-bottom seismic stations may play an essential role in a comprehensive nuclear test ban treaty (CTBT) which allows only a limited number of land stations to be operated by a monitoring nation within a host nation. This stems from the likelihood that ocean-bottom stations, located in international waters, will not be subject to regulation. They would, in effect, be free stations which could be used to monitor all coastal and island areas. Significantly, the world's most tectonically active areas (see Fig. II-1), where evasion schemes are likely to be attempted, are near the deep ocean.[1] Clearly, internal land stations, whose number and location are likely to be restricted by a host nation, are not necessary to monitor these high-seismicity areas. In any event, the available land stations should not be wasted here.

The use of ocean-bottom stations for regional surveillance is predicted, of course, on the ability of such stations to detect and discriminate small explosions from earthquakes. Unfortunately, adequate information is not available to assess the relative performance of ocean-bottom stations in a near-in, or regional, context. Initial experiments in the early 1960's suggested that the ocean bottom may be a high SNR environment.[2-5] However, further studies sponsored by ARPA in the mid-60's indicated that ocean-bottom seismographs (OBSs) would not be as effective as land stations for teleseismic surveillance.[6-8] This conclusion was based largely on the observation that the lower-frequency (<5-Hz) background noise level, measured at several ocean sites by short-period instruments, was much higher than that at land sites. Accordingly, the concept of using ocean-bottom seismographs for teleseismic monitoring was abandoned in the late 1960's. Today, such a judgment may no longer be valid in view of the substantial advances in seismic instrumentation and oceanographic methods for deploying and recovering seafloor devices.

We have recently completed a preliminary review of OBS and marine technology.[9] From this work, it appears that modern digital seismometers rigidly emplaced beneath the seafloor by deep-sea drilling ships, manned submersibles, or remote-controlled manipulator ships could provide low-noise ocean-bottom stations useful for both teleseismic and regional monitoring. In fact, by incorporating modern acoustic data telemetry, it should be possible to have essentially real-time monitoring comparable to that from land stations. The more important scientific advantages of OBS stations, particularly sub-seafloor installations, are summarized in Secs. 1 and 2 below. Figure II-2 shows the primary seismic ray paths on ocean bottom.

1. Seafloor OBSs vs Land Seismograph Stations

(a) Increased Signal Amplitude:– Although most previous OBS experiments have probably not measured the true ground motion on the seafloor because of poor coupling and high background noise, it is clear that signal amplitudes from earthquakes observed on the ocean floor are generally higher than those seen by a land station. For example, the ARPA-sponsored Texas Instruments (T.I.) field tests off the Aleutian Islands showed that OBS-calculated m_b values averaged 0.2 unit greater than land-station calculated values.[7] This was thought to result from the fact that rays traveled a slightly shorter path to the ocean-bottom stations and, more important, they did not propagate through a low-Q continental crust. Also, more-recent work suggests that

47

shallow oceanic paths will show extremely low attenuation compared with continental paths.[10] Oceanic Q values typically exceed 6000 at 20 Hz.

(b) Lower Noise:— Deep-ocean sites are relatively isolated from the sources of background noise likely to affect seismic stations, namely: cultural noise, breaking surf on coastlines, storm microseisms, and local sea surface waves of tidal current effects. In practice, this appears to be the case.[2,5,7] The dominant noise source is believed to be surf microseisms propagating out from the coastline as Rayleigh waves in the water mass and along the water-seafloor interface [Fig. II-2(a)].

TABLE II-1 COMPARISON OF SRO STATION NOISE BACKGROUND WITH OBS OBSERVATIONS [Mean rms Noise Amplitude (mµ)]			
Station/Investigators	Vertical Component		Operational Dates
	Short Period (f_o)	Long Period (f_o)	
SROs[†]			
Albuquerque, N.M.	0.38 (2.86 Hz)	9.56 (25 sec)	1977–
Guam Island	40.25 (2.96 Hz)	11.25 (25 sec)	1977–
New Zealand	28.92 (2.86 Hz)	45.92 (25 sec)	1977–
OBSs			
Asada and Shimamura[10]	≈50 (2.7 Hz)	–	1972–
Francis et al,[12] Francis et al,[13]	≈25 to 50 (8.0 Hz)	–	1972–
Texas Instruments Inc.[6]	≈100 to 300 (1 Hz)	–	1965-1968
Sutton et al.[5]	–	5,000 (15 sec)	1965-1972?
Bradner et al,[4]	≈800 (1 Hz)	≈10,000 (5 to 10 sec)	1964
Ewing and Ewing[2]	≈1 (2 Hz)	–	1959-1961
† Source: Texas Instruments Quarterly Report.[11]			

Table II-1 lists representative noise levels observed on land and on the seafloor. Note that only the early Lamont workers[2] reported short-period noise amplitude levels comparable to those observed on land instruments (i.e., 1-mµ p-p in the 2- to 10-Hz band). Unfortunately, their low-noise observations were not substantiated in the more-extensive field tests carried out by T.I. in the mid-1960's.[6] Noise amplitudes were typically two-orders-of-magnitude greater than those reported earlier (i.e., 100 to 300 mµ at 1 Hz). However, it must be emphasized that these apparent high-noise observations may not have been a true measure of solid earth motions after considering the methods used to make background noise observations. In T.I.'s system and, for that matter, with most systems: (1) the seismometers simply rested on

surficial, unconsolidated seafloor sediments and ooze whose seismo-acoustic properties were not much different than the overlying water mass [Fig. II-2(b): OBS position 1], and (2) these devices used tall vertical frames which protruded into water mass to house their seismometers. These facts suggest that most OBSs have probably recorded ocean-water motion as well as solid-earth ground motion. Significantly, those seafloor OBSs with seismometers[10,12,13] well-coupled to the solid earth and isolated from water-induced motions on the housing frame have shown short-period noise levels approaching the 1- to 10-mμ levels observed at the better land SRO stations today (Table II-1). No studies of long-period seafloor noise other than the preliminary Lamont and Scripps work,[4,5] have been reported to date.

2. Sub-seafloor vs Seafloor OBSs

Additional advantages can be gained for OBSs by implanting the seismometer beneath the seafloor. Some of these are enumerated below.

(a) Better Coupling to the Solid Earth:– The most obvious method for improving the coupling of ocean-bottom seismometers to the solid earth and isolating them from disturbing noise in the ocean water and surficial sediments is to rigidly mount the seismometers beneath the seafloor [Fig. II-2(b): OBS position 2]. Competent sedimentary rocks usually lie within a few tens of meters beneath the seafloor. In fact, the hard igneous rocks of the high-Q oceanic crust are only covered by a few hundred meters of sediment in most areas. A borehole-type OBS installation on or within the oceanic basement (positions 3 or 4) should prove vastly superior to the conventional free-fall devices previously deployed. The signal amplitude can be maximized by adjusting the seismometer case density to improve its acoustic impedance match with the surrounding borehole materials.

(b) Lower Noise:– A buried seismometer will be well-isolated from local noise generated in the ocean water. The air-water and seafloor-water interfaces serve as efficient reflectors which effectively trap any propagating waves in the water [Fig. II-2(c)]. In fact, recent tests in shallow water showed more than a factor-of-10 reduction in local ocean-generated noise on a vertical component seismometer buried only 2 m beneath the seafloor.[14] Also, in a deep-water test conducted aboard the GLOMAR CHALLENGER drilling ship, very low noise levels (<<120 mμ at 10 Hz) were observed beneath the seafloor.[15]

The distant coherent noise propagating in the water mass and surficial sediments should also be markedly attenuated at depths of only a few hundred meters since the shear-wave velocity of the surficial unconsolidated sediments is only about 0.1 to 0.4 km/sec (Ref. 16). This noise, which is generated beneath the breaking waves on beach surfaces, will remain primarily in the waveguide formed between the reflecting seafloor and underlying harder-rock interfaces [Fig. II-2(a)]. Seismometers buried 300 to 600 m beneath the seafloor would be effectively shielded from this dominant source of seafloor noise.

(c) Reduced Signal Contamination:– Seismic signals received at a seafloor OBS travel through the ocean water as well as through the solid earth beneath the station (position 1 in Fig. II-2). Rays reflected from the local air-sea surface interface, as well as shear waves propagating along the soft sediment waveguide, contaminate the direct seismic arrival phases. These arrivals not only introduce apparent complexity in the wave-train coda but they also tend to reduce signal amplitude because of interference effects. By locating the seismometer

in a borehole beneath the seafloor surface, seismic waves entering the overlying water mass and soft sediments will be effectively trapped much like the noise initially generated in the ocean (position 3 and 4).

(d) More - form Crust and Mantle Structure:- The crust and mantle structure beneath the ocean basins is now known to be much simpler than that beneath the continents. The seafloor spreading hypothesis, generally accepted by ocean scientists to account for the formation of the seafloor, predicts that nearly horizontal rock layers underlie most of the deep ocean. Marine geophysical measurements support this hypothesis.

Simple layering implies that large-aperture arrays could be deployed to further improve the SNR by beamforming or velocity filtering. In fact, many of the signal-processing problems caused by the near-field complexity of earth structure at land arrays (e.g., LASA, NORSAR) will not be encountered. By sharply reducing signal-generated coherent noise, a closer approach to the ideal $\sqrt{N}$ SNR enhancement might be realized. The widespread uniformity of earth structure beneath the ocean also implies that much larger arrays than those practical for land installation could be built.

<div align="right">
J. D. Phillips
D. W. McCowan
</div>

B. RELOCATION OF OCEAN-RIDGE EARTHQUAKES

Detailed knowledge of the location of ocean-ridge earthquakes relative to each other and to the ridge's islands, bathymetric features, and magnetic/gravity fields would be useful for geophysical studies as well as nuclear monitoring activities. Unfortunately, conventional methods for determining epicenter locations on ridges may not be adequate to attain the required precision and accuracy in that relatively simple Jeffreys-Bullen[17] or Herrin[18] spherical earth continental-type velocity models are used to calculate travel times and depths.

The computation of the location of earthquakes which are recorded by many observatories distributed in an azimuthally uniform pattern around the epicenter is, of course, insensitive to the errors in any radially symmetric earth velocity model since a travel-time error along one ray-path azimuth is compensated by errors in the opposite sense along reciprocal azimuth ray paths. However, few oceanic-ridge earthquakes are ever teleseismically recorded by such an ideal station distribution due to their generally small magnitude ($m_b \sim 4.0$ to 5.0). Typically, only those stations along a nearby continental margin record the smaller events ($m_b < 4.5$). This fact coupled with the known higher-velocity, 2-dimensional structure beneath ridges at shallow depths (< 200 km), compared to continents, means station azimuth-dependent errors are likely. Epicenter location and depth errors can be expected to be biased along the azimuth toward the greatest number of recording stations.

This biasing effect of epicenter positions was recently demonstrated for the central mid-Atlantic ridge by comparing the epicenter distribution with the known tectonic axis along median valley and transform faults.[19] A markedly skewed arrangement showing wide scatter was observed. The epicenters were generally located to the north and west of the tectonic axes. This distribution was attributed to the "slowness" of the JB model since most of the recording stations were located to the northwest in North America.

A more-realistic earth-velocity model has recently been devised to account for both the higher velocity and two-dimensional nature of ocean-ridge structure. For the ridge crest region down to a depth of 78 km, the velocity structure proposed by Steinmetz et al.[20] was used.

This structural model which includes shallow-depth velocity inversions is based on seismic refraction results from the mid-Atlantic ridge between 45° and 40°N latitudes and petrologic considerations. For the deep-ridge structure and the continental regions, the Herrin velocity model[18] was used. The ridge axis water depth was taken as 3 km. Ray tracing was then done to calculate travel times and epicentral distances for earthquakes occurring on the ridge axis at depths of 3, 33, 96, and 200 km (Refs. 21 and 22). Figure II-3 shows comparisons of the differences in travel times between the "fast" oceanic-ridge model proposed here and the "slow" JB model. Note that the largest differences are for the surface depth event. This might be expected since the ridge model shows very high velocity layers (Vp ≈ 7.7 to 8.0 km/sec) within 5 km of the surface. In fact, true mantle-like layers (Vp > 8 12) are only 75 km below the surface. The JB model puts these layers at 33 and 160 km, respectively.

To test the efficacy of the model to better locate earthquakes, ten events which occurred along well-charted portions of the north mid-Atlantic ridge during an arbitrary period (March-September 1964) were analyzed (Fig. II-4). The median valley and transform fault axes here are known with an accuracy of ±2 km. Table II-2 summarizes the relocation parameters of epicenters shown in Fig. II-4 as well as for other nearby events.

Careful examination of Table II-2 reveals that, for those location solutions which were depth convergent, the new depths of the three larger-magnitude events (>4.8) became more shallow while the epicenter moved toward the ridge axis (Fig. II-4). In contrast, the smaller-magnitude events showed increased depths; however, their epicenters also moved closer to the ridge axes. Since most oceanic-ridge earthquakes are small and are believed to occur above the base of the lithosphere (~110 km thick), a test was made to determine the maximum epicenter relocation effect by depth constraining all solutions to an arbitrary depth of 113 km. The open circles in Fig. II-4 show these relocations. Note that in all cases, save one (ISC event 829), the epicenters moved toward the ridge axis and in several cases they moved exactly onto the axis! Although these results suggest the new velocity model better approximates the true velocity structure beneath ridges than does the JB model, further statistical evaluation of the general applicability of the model is required. Relocation of a large number of events over a more extensive portion of the ridge crest would be appropriate.

J. D. Phillips   L. C. Lande
R. E. Needham   D. W. McCowan
R. S. Sheppard

C.   A NOTE ON ELLIPTICITY CORRECTIONS FOR SURFACE-REFLECTED PHASES

Dziewonski and Gilbert[23] using addition theorem for Legendre functions presented an efficient and accurate method of calculation of ellipticity corrections.

They proposed to evaluate the ellipticity correction according to the formula:

$$\delta t = \sum_{m=0}^{2} \tau_m(\Delta) \, P_{2,m}(\cos \nu_o) \cos m\xi \tag{II-1}$$

where ν_o is the colatitude of the source, ξ is the azimuth from the source to the receiver, Δ is the epicentral distance, and

TABLE II-2

RELOCATED EPICENTERS FOR OCEAN-RIDGE EARTHQUAKES

Depth Convergent Solutions

Date	JB$_{ISC}$					Ridge				ISC No.	No. of Stations
	Time	Latitude (°N)	Longitude (°W)	Depth	m$_b$	Latitude (°N)	Longitude (°W)	Depth	Time		
03/04/64	02:58:31.2	43.60	28.99	49	4.5	43.66	28.99	60	02:58:35.2	822	39
06/05/64	04:44:53.4	47.60	27.33	82	4.7	47.60	27.34	90	04:44:57.2	2842	64
07/13/64	16:22:27.5	53.90	35.13	39	4.2	54.03	35.35	60	16:22:33.4	3607	21
08/17/64	09:07:06.5	51.92	30.08	64	4.8	51.85	30.02	81	09:07:10.6	4107	61
08/17/64	22:47:31.5	52.03	30.09	25	5.0	52.08	30.13	1	22:47:31.8	4124	63
08/22/64	17:04:29.7	51.94	30.15	19	5.0	51.96	30.19	16	17:04:31.8	4204	64
08/26/64	03:18:43.7	52.12	30.12	28	5.2	52.06	30.14	0	03:18:43.2	4269	113

Depth Constrained Solutions

Date	JB$_{ISC}$					Ridge				ISC No.	No. of Stations
	Time	Latitude (°N)	Longitude (°W)	Depth	m$_b$	Latitude (°N)	Longitude (°W)	Depth	Time		
03/04/64	01:17:21.2	43.40	29.07	33	4.5	43.33	28.94	113	01:17:31.8	819	10
03/04/64	02:58:31.2	43.60	28.99	49	4.5	43.56	28.91	113	02:58:39.9	822	39
03/04/64	12:59:11.5	42.70	29.00	33	4.2	42.75	28.93	113	12:59:22.8	829	16
03/04/64	16:16:30.8	43.60	29.22	33	4.8	43.72	29.14	113	16:16:42.1	831	28
06/05/64	04:44:53.4	47.60	27.33	82	4.7	47.60	27.30	113	04:44:59.3	2842	64
07/13/64	16:22:27.5	53.90	35.13	39	4.2	53.99	35.30	113	16:22:38.2	3607	21
08/17/64	09:07:06.5	51.92	30.08	64	4.8	51.86	29.96	113	09:17:13.6	4107	61
08/17/64	22:47:31.5	52.03	30.09	25	5.0	52.08	29.90	113	22:47:43.2	4124	63
08/22/64	17:04:29.7	51.94	30.15	19	5.0	51.90	29.98	113	17:04:41.9	4204	64
08/26/64	03:18:43.7	52.12	30.12	28	5.2	52.21	30.11	113	03:18:55.3	4269	113

$$\tau_m(\Delta) = p^{-1} \int_0^\Delta \eta^3 \frac{dv}{dr} \, \epsilon\lambda_m(\Theta) \, d\Theta - \sum_j{}' \left\{ \epsilon\lambda_m(\Theta) \left[(\eta^2 - p^2)^{1/2} \right] \right\}_j$$

$$\mp \sum_k{}' \left\{ \epsilon\lambda_m(\Theta) \left[(\eta_\pm^2 - p^2)^{1/2} \right] \right\}_k \tag{II-2}$$

where

$$\lambda_m(\Theta) = -\frac{2}{3} P_{2,m}(\cos\Theta)$$

and the remaining symbols are standard (cf. Ref. 24, pp. 173-176). The sums represent the effect of discontinuities in the velocity structure on transmitted (j) and reflected (k) rays.

The advantage of this approach is that accurate results can be obtained by evaluating only three integrals [Eq. (II-2)] for a particular epicentral distance and the species of ray. Tables in Ref. 23 give values of $\tau_m(\Delta)$ for eight commonly reported body-wave phases.

Here, we purport to show how the tabular material of Ref. 23 can be easily extended to evaluate ellipticity corrections for surface-reflected phases such as PP, PS, PSS, $(ScS)_2$, etc.

Obviously, Eq. (II-2) could be directly applied to evaluation of ellipticity corrections for composite phases by integrating along the entire ray path, but this procedure would be needlessly time consuming. For a phase reflected at a distance Δ_1 and observed at a distance Δ_2, the integral in Eq. (II-2) can be represented by a sum of the integrals

$$\int_0^{\Delta_2} = \int_0^{\Delta_1} + \int_{\Delta_1}^{\Delta_2} \quad ;$$

the terms corresponding to the effect of the discontinuities are omitted for brevity. Each of the integrals corresponds to the ellipticity corrections accumulated over the first and second legs of the path, respectively.

By changing the variable Θ to $\nu + \Delta_1$, the second integral now has the limits $(0, \Delta_2 - \Delta_1)$. With the use of some simple trigonometric transformations, it is easy to show that

$$\lambda_m(\nu + \Delta_1) = \sum_{k=0}^2 A_{mk}(\Delta_1) \cdot \lambda_k(\nu) \tag{II-3}$$

where

$$A = \begin{bmatrix} \frac{1}{4}(1 + 3\cos\Delta_1) & -\frac{\sqrt{3}}{2}\sin 2\Delta_1 & \frac{\sqrt{3}}{2}\sin^2\Delta_1 \\[2ex] \frac{\sqrt{3}}{2}\sin 2\Delta_1 & \cos 2\Delta_1 & -\frac{1}{2}\sin 2\Delta_1 \\[2ex] \frac{\sqrt{3}}{2}\sin^2\Delta_1 & \frac{1}{2}\sin 2\Delta_1 & \frac{1}{2}(1 + \cos^2\Delta_1) \end{bmatrix} \quad .$$

By substituting Eq. (II-3) into (II-2), we find that the coefficients τ corresponding to the ellipticity corrections accumulated over the entire path of the ray are

$$\tau_m(\Delta_2) = \tau_m(\Delta_1) + \sum_{k=0}^{2} A_{mk}(\Delta_1)\, \tau_k(\Delta_2 - \Delta_1) \quad ; \tag{II-4}$$

$\tau_k(\Delta_2 - \Delta_1)$ is the ellipticity correction coefficient for a surface-focus, single-leg phase observed at $\Delta = \Delta_2 - \Delta_1$.

Equation (II-4) can be easily generalized for an arbitrary number of surface reflections, with the individual legs corresponding to either P- or S-wave type.

<div style="text-align:right">A. M. Dziewonski</div>

D. CORRESPONDING SHEAR STRAIN AND Vp ANOMALIES IN THE TONGA DEEP-EARTHQUAKE ZONE

In the previous SATS,[25] Fitch and Jackson presented velocity anomaly patterns computed from differential residuals from earthquake locations relative to a master. To stimulate geophysical interest, each pattern and the corresponding relative locations were projected onto a vertical plane normal to the strike of the seismic zone. Each pattern may be distorted by the defocusing effect of the high-velocity slab, and each velocity increment in a given pattern may be in error by, say, 100 percent. Of particular interest is the pronounced high-velocity lobe in the down-dip direction of the deep Tonga seismic zone as well as the overall simplicity of that pattern. A refined version of that anomaly pattern is presented in Fig. II-5. The master earthquake is at a depth of about 650 km, which is within 50 km of the deepest earthquakes located in this zone. Figure II-6 shows that if the same group of earthquakes are relocated with respect to a master chosen from among the shallower events in this group, the resulting anomaly pattern is almost perfectly out of phase with the pattern for the deeper master. Figure II-7 shows that the anomaly in down-dip direction is negative if one of the shallower earthquakes is used as a master, in this case the master is located at a depth of about 530 km. Apparently, variations in near-source velocity structure as seen from the shallower master are opposite in sense to those seen by the deeper master.

This out-of-phase relationship cannot be the result of the different configuration of the secondary events with respect to each master or the velocity increase with depth expected from self-compression alone. Both of these possibilities are eliminated by computing anomaly patterns from synthetic data that simulate both the statistics of the real data and the real distributions of stations and sources. A Herrin mantle and JB core were chosen for this simulation. The patterns for deeper and shallower masters are compared in Fig. II-8. The out-of-phase relationship so obvious in Fig. II-6 is not present. Furthermore, the patterns from synthetic data are more complex than those from real data, thus supporting a claim that the random errors in the real data have been effectively suppressed.

The out-of-phase relationship and other published evidence strongly suggest that a major phase boundary exists somewhere between the two masters. In situ compressional velocities for this seismic zone are high by 5 to 10 percent for master earthquakes located at depths of about 600 km and deeper.[26] McGarr[27] showed that there is a dramatic increase in the release of shear strain at a depth of about 600 km in this seismic zone. His results are based on the conversion of published m_b values to seismic moments. The correlation in depth between velocity and shear-strain anomalies strongly suggests a cause-and-effect relationship, the

obvious one being that the shear strain released by these deep earthquakes is generated by a change to a denser mineral assemblage.

<div align="right">
T. J. Fitch
J. Jackson[†]
</div>

E. DETECTION OF MULTIPLE EXPLOSIONS USING SURFACE WAVES AT MAIO

We are investigating the use of surface waves to detect multiple explosions from Eastern Kazakh. Although surface waves are longer period than body waves, they are broader band in frequency and well dispersed. Therefore, they are well suited to pulse-compression schemes such as matched filtering, which has been extensively used in the past[28] to detect interfering Rayleigh waves. At teleseismic distances less than 25°, the short-period body waves are often quite complex due to travel-time triplications produced by the upper-mantle velocity structure. This often makes it difficult to use short-period data for detecting multiple shots, whereas surface waves at such distances suffer no such degradation.

Table II-3 lists the PDE parameters for four Eastern Kazakh explosions with well-recorded surface waves at the Meshed SRO (MAIO) which is ~19° from the epicenters. Events 3 and 4 in the table have origin times and distances which differ respectively by 5 sec and 56 km. Figure II-9 shows the epicenters and great-circle ray paths toward MAIO for these two events.

TABLE II-3						
PDE PARAMETERS FOR FOUR EASTERN KAZAKH EXPLOSIONS						
Event	Date	Latitude (°N)	Longitude (°E)	Origin Time (GMT)	m_b
1	7/4/76	49.92	78.95	2:56:58.0	5.3
2	8/28/76	49.97	79.00	2:56:58.0	5.8
3	10/29/77	49.84	78.17	3:06:59.7	5.5
4	10/29/77	50.06	78.91	3:07:02.9	5.6

Our scheme for the detection of multiple explosions uses least-squares filters to shape the one Rayleigh wave to another. The filter is interpreted to be the transfer function in time which, when convolved with the first wave, produces the second wave with least-squares error.

Figure II-10 shows the Rayleigh waveforms (Z component) at MAIO for Events 1 and 2 and the least-squares filter 50 points long which, when convolved with Event 1, yields Event 2 in a least-squares sense. The filter was obtained by solving the normal equations

$$\overline{\overline{R}}\,\overline{f} = \overline{d} \qquad\qquad (II\text{-}5)$$

where $\overline{\overline{R}}$ is the autocorrelation matrix of Event 1, and $\overline{d}$ is the cross-correlation vector between Events 1 and 2 evaluated at 50 lag values, the same length as $\overline{f}$. This equation is the classic least-squares Wiener-filter equation in the time domain, which is rapidly solved by the Levinson recursion scheme.[29] Because of the correlations used in the equation, this scheme is analogous to matched filtering but more versatile.

[†] Cambridge University, Cambridge, England.

The filter in Fig. II-10 is a very simple pulse of negative amplitude indicating that the Rayleigh wave for Event 2 is very similar to that of Event 1 except for a polarity change, which is due to the phase difference within the group delay envelopes of each event.

Figure II-11 shows the interference pattern of Rayleigh waves from Events 3 and 4 compared with Event 1. The least-squares filter to shape Event 1 to the composite waves of Events 3 and 4 is more complex than the filter in Fig. II-10, primarily due to the two negative pulses separated by about 27 sec. This indicates that the composite Rayleigh wave is well approximated by a weighted sum of two Rayleigh waves of Event 1.

As a check on the stability of the filter shapes in Figs. II-10 and II-11, two extra lags were introduced in each case to delay the position of the negative spikes within the 50-point length filter. The new computed filters are superposed over the old ones with the lags removed, and are displayed in Fig. II-12(a-b). The filter shapes in each case are very consistent, and in Fig. II-12(a) the two negative spikes are considered reliable.

The time delay at MAIO between Events 3 and 4 can be inferred approximately from Fig. II-9. Assuming a group velocity of ~3.0 km/sec at a 20-sec period from Eastern Kazakh to MAIO gives a time shift of 18.7 sec based on the difference in great-circle path lengths. This, added to the difference in origin time of 5.1 sec, gives ~24 sec which is quite close to the 26- to 27-sec delay between the negative spikes in Fig. II-12(a), considering the inaccuracies in PDE locations and origin times.

Unfortunately, the surface waves generated by this explosion pair were not of sufficient amplitude to be observable at the other, more-distant SRO stations, and thus we are unable to unequivocally verify the calculated separation between surface-wave arrivals through its variation with azimuth. The short-period recording of the double event observed at MAIO is too complex to interpret, and this may be a reason for testing this method further with azimuthally distributed surface waves from multiple earthquakes and explosions when they occur.

<div align="right">
C. W. Frasier
R. G. North
</div>

F. SPECTRAL CHARACTERISTICS OF RAYLEIGH WAVES FROM AN AFTERSHOCK SEQUENCE

In a previous SATS,[30] we described an unique dataset of surface waves recorded at Meshed SRO from an aftershock sequence in the Kuril Islands. The relocated epicenters are constrained to an area of 80 × 50 km in extent and, in addition, over 80 percent of the events had pP phases indicating a consistent depth for the sequence of 45 to 55 km. Surface-wave magnitudes measured at Meshed range from 4.3 to 7.3. We have attempted, without success, to determine fault-plane solutions for these events from WWSSN data: all we can say is that the few first arrivals observed were uniformly compressional, indicating thrust faulting. This is consistent with the tectonics of the area.

We have considerably refined our spectral-estimation technique, using the time-variable filtering technique[31] to remove both severe multipathing and the effect of multiple events. The amplitude spectra obtained appear (curiously) to divide into two distinct types, shown in Figs. II-13 and II-14. The SRO instrument response has not been removed, since we are only interested in spectral comparisons. Type I events (Fig. II-13) have a pronounced spectral hole at 0.025 Hz, whereas those of type II (Fig. II-14) have two much-less-well-developed such "holes." The similarity of the spectra within each group is remarkable. Because of the rapid falloff of

the SRO instrument response at periods less than 10 sec, seismic scaling effects will only be apparent for events with corner frequencies greater than 0.1 Hz, corresponding to those with $M_s > 6.0$ on the basis of the ω-square law.[32] This explains the almost identical spectra for the type II events, all of $M_s \leqslant 6.3$, and we do indeed see an enhanced long-period content for the largest type I events.

We have computed theoretical amplitude spectra for a pure-dip slip event at 50 km depth in a Gutenburg continental model, and find that the spectral hole at a 40-sec period is indeed predicted. We have attempted to find some explanation for the absence of this feature in the type II events, but in terms of location, depth, and (as far as we can tell) mechanism, they are identical with those of type I. We intend to study the short-period P-wave signals from the two classes of events to see whether these also differ.

We have recomputed spectral amplitude ratios for the largest events and find good agreement with the ω-square (Ref. 32) law of seismic scaling. Predicted and observed ratios are shown in Fig. II-15. We also attempted to measure spectral phase differences between events, but were unsuccessful, probably because the spatial separation between the larger events introduces a frequency-dependent phase delay for which we cannot correct without a more-detailed knowledge of the dispersion characteristics of the source region.

R. G. North

REFERENCES

1. J. Evernden, "Study of Seismological Evasion: Part I General Discussion of Various Evasion Schemes," Bull. Seismol. Soc. Am. 66, 245 280 (1976).

2. J. Ewing and M. Ewing, "A Telemetering Ocean-Bottom Seismograph," J. Geophys. Res. 66, 3863-3878 (1961).

3. R. A. Arnett and T. W. Newhouse, "Ocean-Bottom Seismograph," Proc. IEEE 53, 1899-1905 (1965).

4. H. Bradner, J. G. Dodds, and R. E. Foulks, "Investigation of Microseism Sources with Ocean-Bottom Seismometers," Geophysics 30, 511-526 (1965).

5. G. H. Sutton, W. G. McDonald, D. D. Prentiss, and S. N. Thanos, "Ocean-Bottom Seismic Observatories," Proc. IEEE 53, 1909-1921 (1965).

6. "Kurile Islands Experiment, Ocean-Bottom Seismographic Experiments," Final Report, Texas Instruments Incorporated (30 August 1967).

7. Signal and Noise Analysis Report, "Aleutian Islands Experiment, Ocean-Bottom Seismographic Experiments," Texas Instruments Incorporated (31 October 1968).

8. "Ocean-Bottom Seismograph Production and Gulf of Mexico Data Analysis," Final Report, Texas Instruments Incorporated (31 July 1968).

9. J. D. Phillips and D. W. McCowan, "Ocean Bottom Seismometers for Nuclear Monitoring and Research: A Reassessment," Technical Note, Lincoln Laboratory, M.I.T. (in preparation).

10. T. Asada and H. Shimamura, "Observations of Earthquakes and Explosions at the Bottom of the Western Pacific: Structure of the Oceanic Lithosphere Revealed by Longshot Experiment," Am. Geophys. Union Monograph 19, 135-153 (1976).

11. "Vela Uniform Evaluation and Automatic Processing Research," Quarterly Report No. 4, Texas Instruments Incorporated (3 October 1977).

12. T. J. G. Francis, I. T. Porter, R. D. Land, P. J. Osborne, J. E. Pooley, and P. K. Tomkins, "Ocean Bottom Seismograph," Marine Geophys. Res. 2, 195-213 (1975).

13. T. J. G. Francis, I. T. Porter, and J. R. McGrath, "Ocean-Bottom Seismograph Observations on the Mid-Atlantic Ridge near Lat. 37°N," Geol. Soc. Am. Bull. 88, 664-677 (1977).

14. G. Purdy, Woods Hole Oceanographic Institution, personal communication (1978).

15. R. Stephens, University of Cambridge, personal communication (1978).

16. E. L. Hamilton, "Shear Wave Velocity Versus Depth in Marine Sediments; A Review," Geophysics 41, 997-1015 (1976).

17. H. Jeffreys and K. E. Bullen, "Seismological Tables," British Association, Gray-Milne Trust (1940).

18. E. Herrin, "1968 Seismological Tables for P Phases." Bull. Seismol. Soc. Am. 58, 1193 (1968).

19. Seismic Discrimination SATS, Lincoln Laboratory, M.I.T. (30 September 1977), pp. 48-49, DDC AD-A050584.

20. L. Steinmetz, R. B. Whitmarsh, and V. S. Moreira, "Upper Mantle Structure Beneath the Mid-Atlantic Ridge North of the Azores Based on Observations of Compressional Waves," Geophys. J. R. Astr. Soc. 50, 353-380 (1977).

21. B. R. Julian, "Ray Tracing in Arbitrarily Heterogeneous Media," Technical Note 1970-45, Lincoln Laboratory, M.I.T. (31 December 1970), 17 pp., DDC AD-720795.

22. S. C. Solomon and B. R. Julian, "Seismic Constraints on Ocean-Ridge Mantle Structure: Anomalous Fault-Plane Solutions from First Motions," Geophys. J. R. Astr. Soc. 38, 265-285 (1974).

23. A. M. Dziewonski and F. Gilbert, "Effect of Small, Aspherical Perturbations on Travel Times and a Re-examination of the Corrections for Ellipticity," Geophys. J. R. Astr. Soc. 44, 7-17 (1976).

24. K. E. Bullen, Introduction to the Theory of Seismology, 3rd Edition (Cambridge University Press, London, 1965).

25. Seismic Discrimination SATS, Lincoln Laboratory, M.I.T. (30 September 1977), pp. 47-48, DDC AD-A050584.

26. T. J. Fitch, "In situ P-wave Velocities in Deep Earthquake Zones of the SW Pacific: Evidence for a Phase Boundary Between the Upper and Lower Mantle," in Island Arcs Deep Sea Trenches and Back-Arc Basins, M. Talwani and W. C. Pitman, III, Eds. (American Geophysical Union, Washington, 1977), pp. 123-136.

27. A. McGarr, "Seismic Moments of Earthquakes Beneath Island Arcs Phase Changes and Subduction Velocities," J. Geophys. Res. 82, 256-264 (1977).

28. J. Capon, R. J. Greenfield, and R. T. Lacoss, "Long-Period Signal Processing Results for the Large Aperture Seismic Array," Geophysics 34, 305-329 (1969), DDC AD-694326.

29. N. Levinson, "The Wiener RMS (Root Mean Square) Error Criterion in Filter Design and Prediction," J. Math.Phys. 25, 261-278 (1947).

30. Seismic Discrimination SATS, Lincoln Laboratory, M.I.T. (31 March 1977), DDC AD-A045453/8.

31. M. Landisman, A. Dziewonski, and Y. Sato, "Recent Improvements in the Analysis of Surface Wave Observations," Geophys. J. R. Astr. Soc. 17, 369-403 (1969).

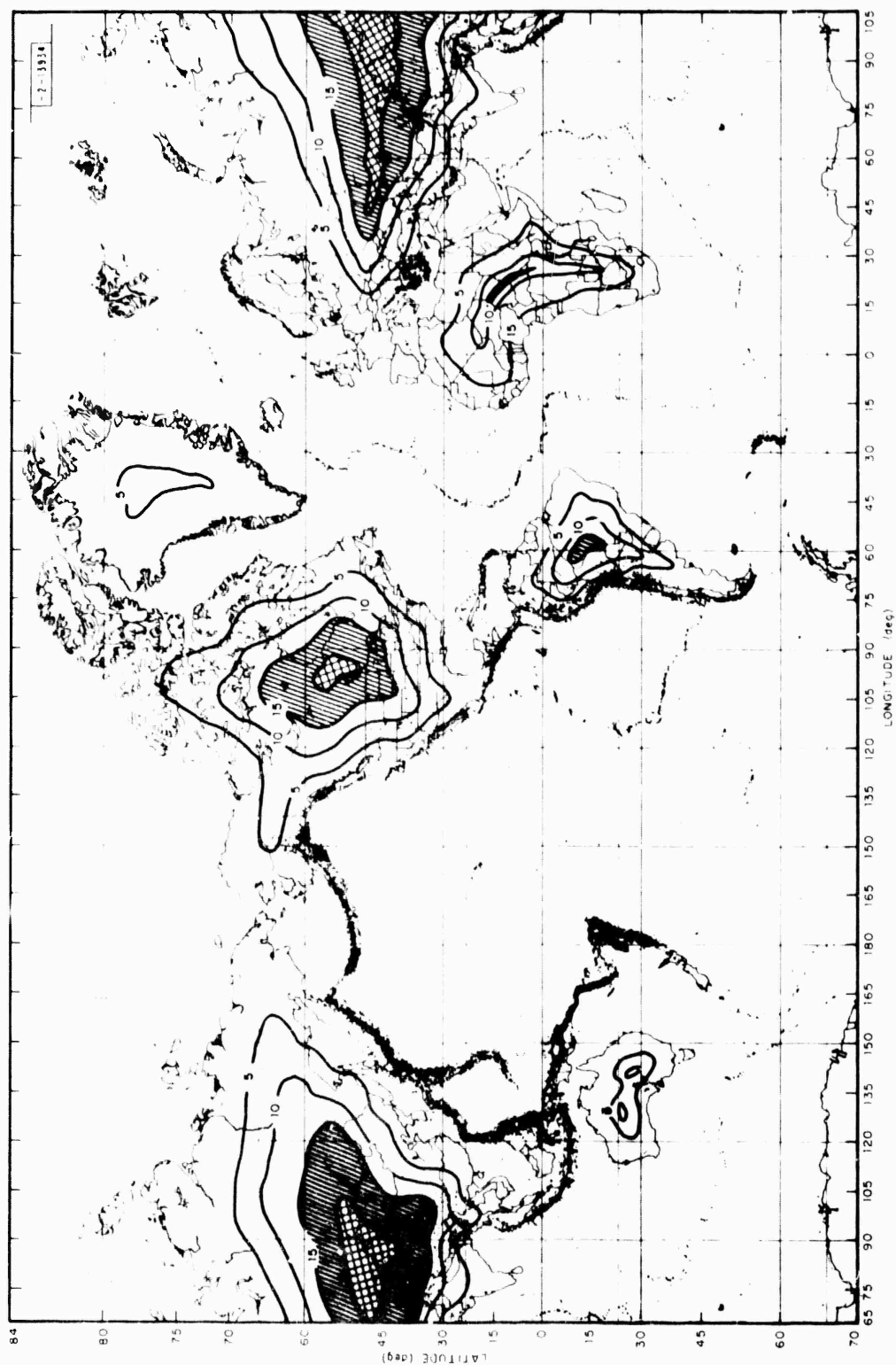32. K. Aki, "Scaling Law of Seismic Spectrum," J. Geophys. Res. 72, 1217-1231 (1967).

Fig.II-1. Chart showing world seismicity 1963-1972 and distance of all land areas, except Antarctica, from deep-ocean international waters. Contours are in 5° intervals; hatched and crosshatched areas show regions greater than 15° (1665 km) and 20° (2220 km), respectively, from deep-ocean areas. Note that nearly entire earth's surface is less than 20° from deep ocean and that virtually all major seismicity zones are less than 5° from deep ocean.
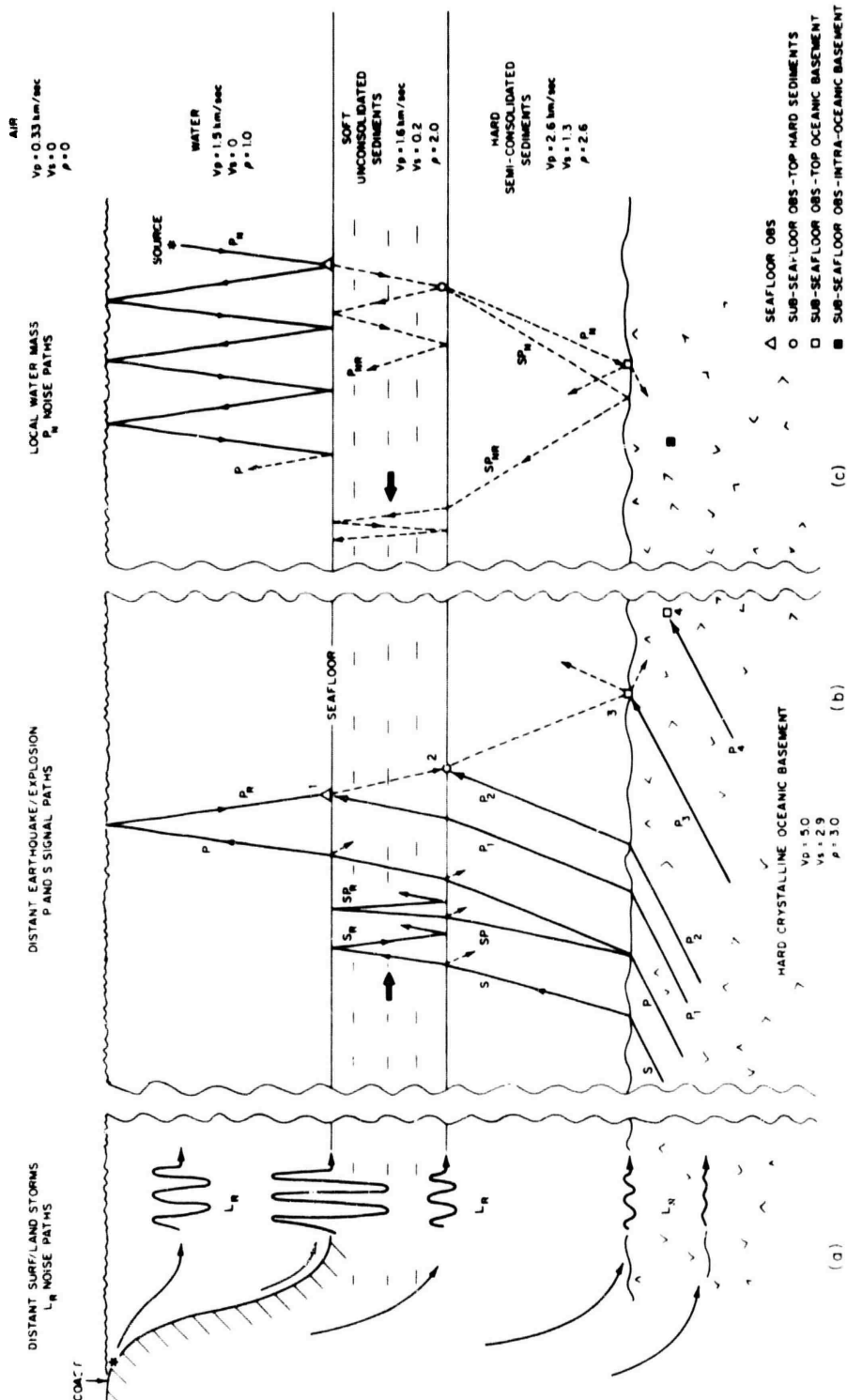
Fig. II-2. Schematic representation of seismic ray paths for ocean-bottom environment. Strong signal ray paths are shown by solid lines in center portion of figure; weaker paths are dashed and dotted. P and S arrivals from distant sources are shown at bottom. Magnitude of microseismic noise, which propagates as Rayleigh waves from coastline along various interfaces, is shown by waveform amplitude at left. Paths for local noise generated in water mass (currents, swells, ships, storms, internal waves) are shown to right. Propagation of trapped shear waves in soft, surficial seafloor sediment layer is shown by heavy arrows.
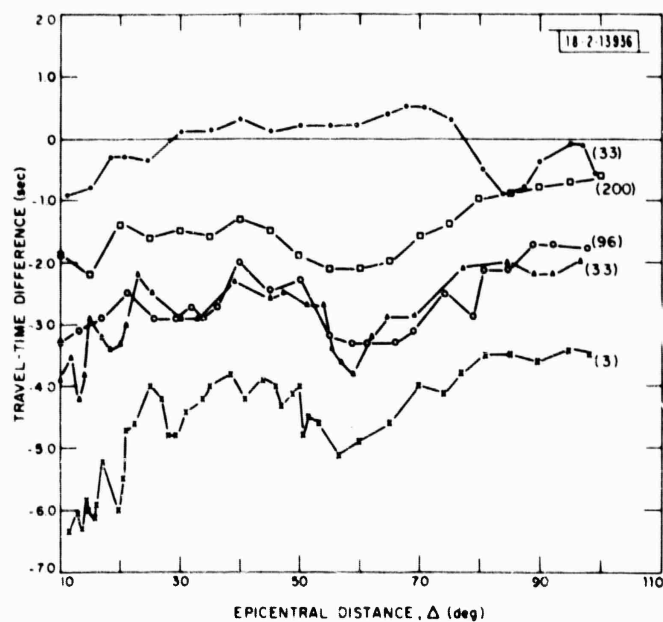
Fig. II-3. Comparison of travel-time difference for new ocean-ridge velocity model and JB model. Uppermost curve shows differences between travel times given in JB Tables at an earthquake depth of 33 km, and those calculated using ray-tracing methods of Julian.[21] Small difference attests to accuracy of ray-tracing method. Four lower curves show travel-time differences for earthquakes at depths (km) indicated.
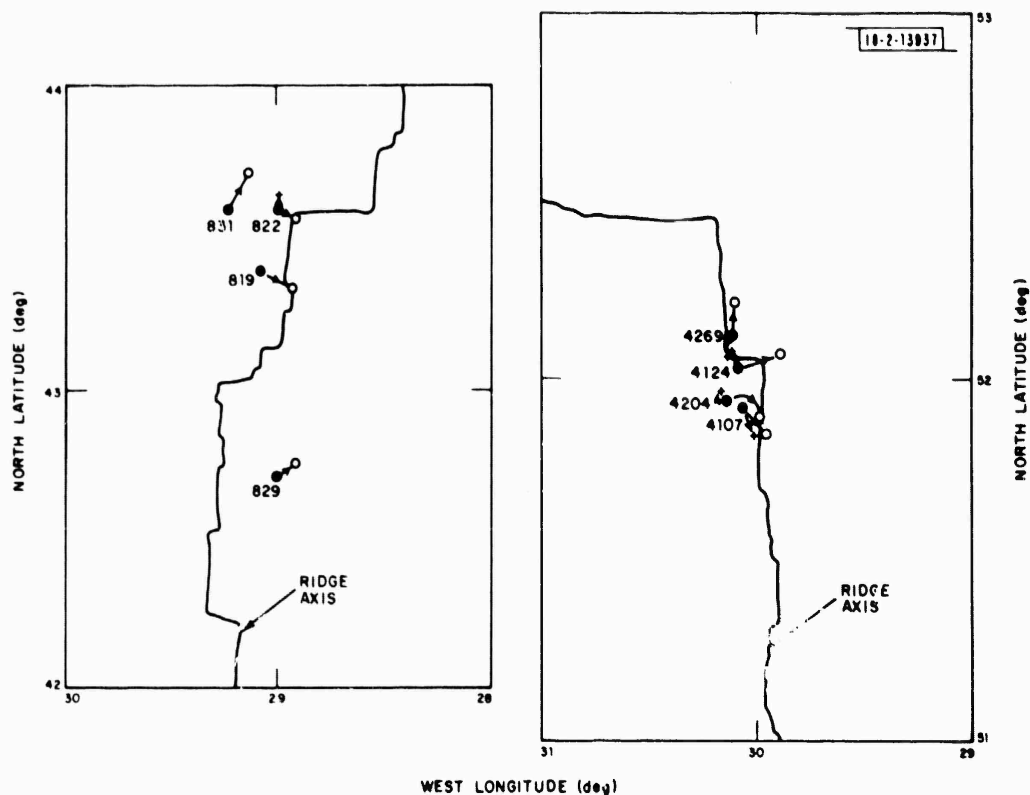
Fig. II-4.   Charts showing relocation of mid-Atlantic ridge earthquakes; quartered circles indicate ISC-computed epicenters and their identifying number, crosses show relocated positions which were depth convergent.   Open circles show relocated epicenter whose depths were constrained to 113 km.   Continuous line delineates axes of median valley (northerly trending segments) and transform faults (easterly trending segments) as determined from high-resolution bathymetric surveys.

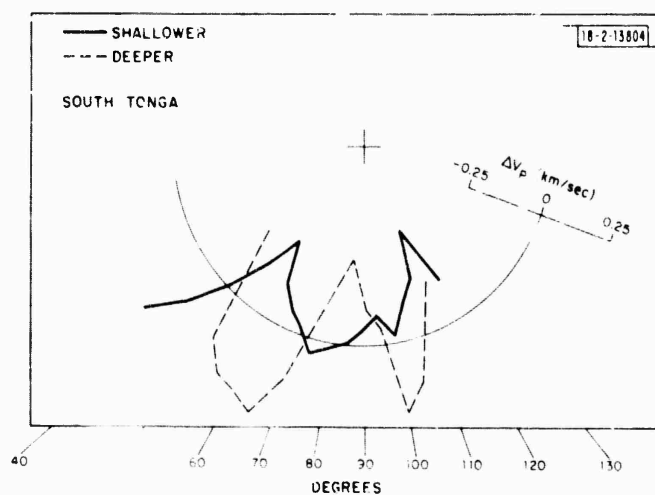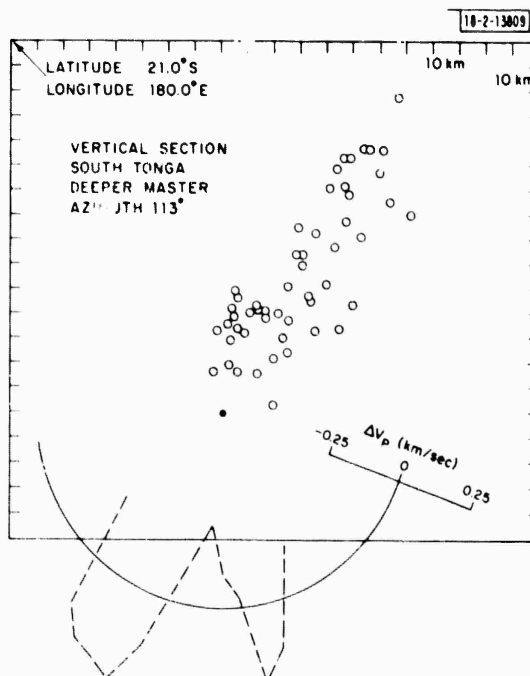Fig. II-5. Velocity anomaly pattern, deep Tonga master.

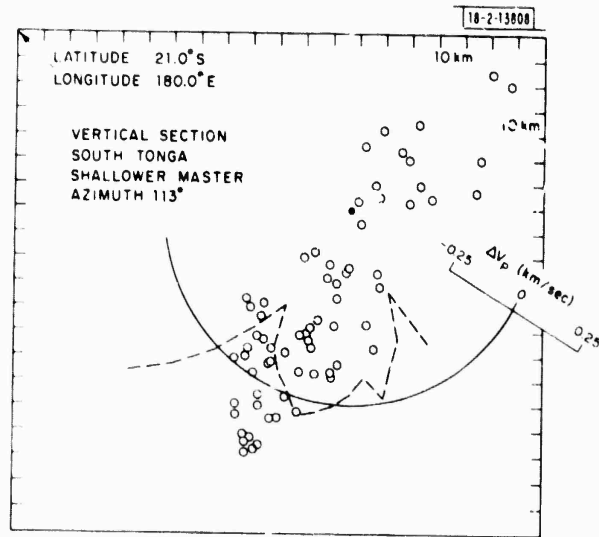Fig. II-6. Comparison oi maly patterns from deeper and shallower masters.

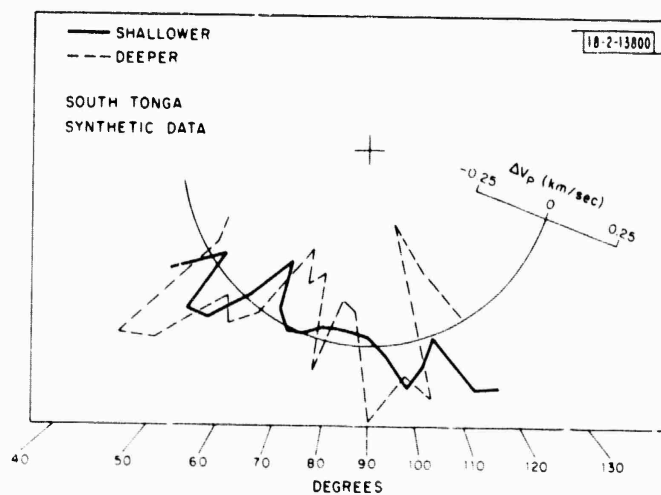Fig. II-7.   Velocity anomaly pattern shallower Tonga master.

Fig. II-8.   Comparison of anomaly patterns from synthetic data (complement to Fig. II-6).
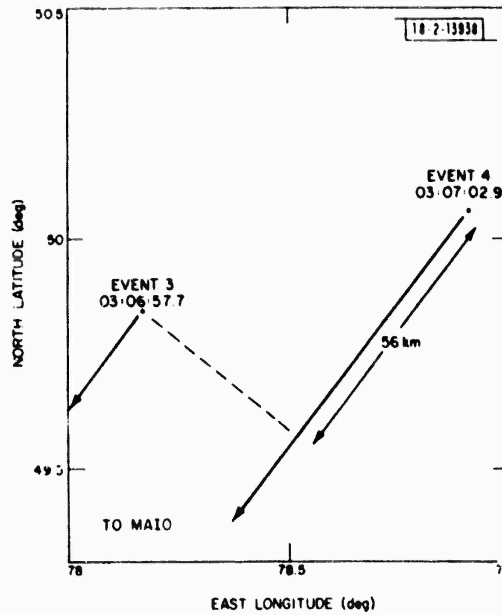
Fig. II-9. Map of epicenters in Eastern Kazakh for Events 3 and 4 in Table II-3, taken from PDE listings. Difference in great-circle path lengths to MAIO and origin times suggests a difference in group arrival time at 20-sec periods of ~24 sec at MAIO.
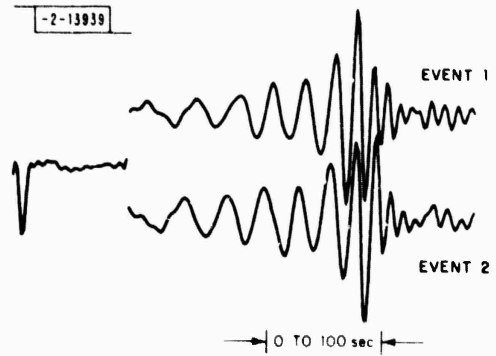
Fig. II-10. Rayleigh waves (Z component) at MAIO for Events 1 and 2 in Table II-3. Least-squares filter to shape Event 1 to 2 is to left.
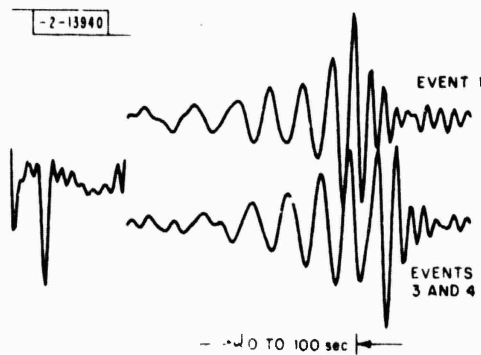
Fig. II-11. Rayleigh waves (Z component) at MAIO for Event 1 and sum of Events 3 and 4 in Table II-3. Least-squares filter to shape Event 1 to combination of Events 3 and 4 is to left.

Fig. II-12. Filters at different lags: (a) to shape Event 1 to sum of Events 3 and 4, and (b) to shape Event 1 to 2.

Fig. II-13. Rayleigh-wave amplitude spectra of type I, Kuril Island earthquakes observed at Meshed SRO.

Fig. II-14. Same as Fig. II-13, type II spectra.

Fig. II-15. Spectral amplitude ratios, observed and predicted, for two earthquake pairs of Kuril Island sequence.

66

III. COMPUTER SYSTEMS
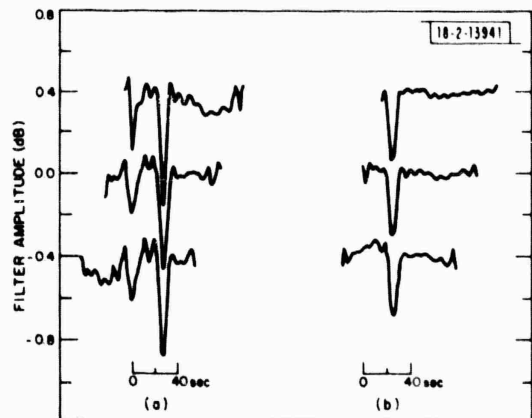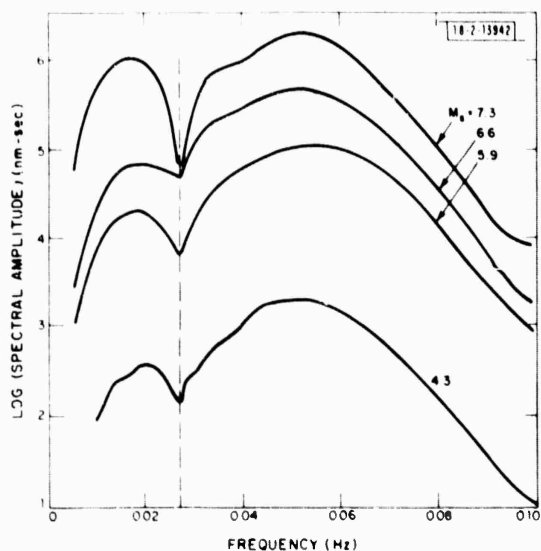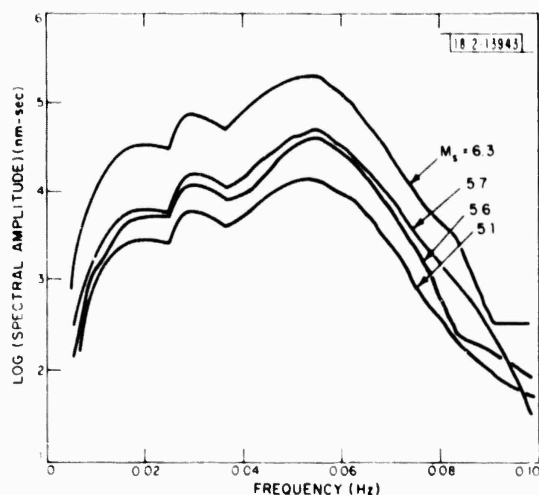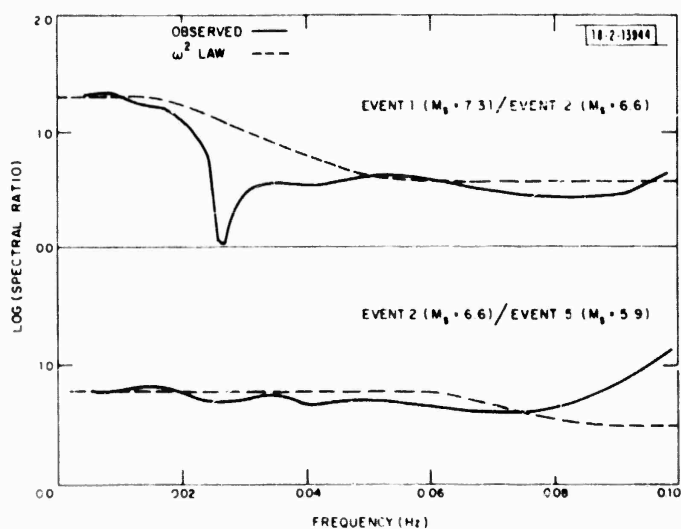
A. PDP-11 COMPUTER FACILITY

A steady increase in computer usage has put an increasing strain on our PDP-11 computer facilities. New hardware purchases and a continuing effort to improve existing software have been made to try to relieve this strain.

1. New Hardware

The new hardware acquisitions include a cache memory system, two new 1600-bpi tape drives, and a 300-Mbyte disk.

The cache memory system is designed to decrease memory access time and thereby increase processor throughput. Its installation has resulted in a 30- to 40-percent increase in processor throughput, depending on the type of load on the system. It has performed flawlessly since the first day of installation.

The new 300-Mbyte disk was acquired to meet the dramatic increase in the amount of file storage required by our users. Our existing disk system with 80 Mbytes of storage was much too small to deal with the large seismic data bases our users require.

Unfortunately, the addition of the new disk caused some unexpected problems in our overall system. The increased load on the UNIBUS revealed some design flaws in some of the other peripheral devices. In particular, we found that the existing TU10 tape drive controller and the VDH ARPANET interface could not function with the increased competition for the UNIBUS. Data overrun errors on both devices had disastrous consequences which made them almost unusable. Several measures have been taken to overcome this problem. The VDH hardware and software have been modified to handle data overrun errors more intelligently. As a temporary measure, the 80-Mbyte Diva disk system has been disconnected to reduce UNIBUS contention. Further improvements in the software drivers for the tape drives and disk are needed to completely solve the problem. It is our belief that the newly purchased 1600-bpi tape drives will have fewer problems because of improved controller design.

In addition to the hardware problems, the 300-Mbyte disk has forced us to rewrite our file system backup procedures. The existing UNIX software for backing up file systems is incapable of handling 300-Mbyte file systems.

The 1600-bpi tape drives were obtained to handle the increasing tape usage on our system. The planned shutdown of the PDP-7 computers will leave the PDP-11 system as the only way to access the seismic data in our extensive tape library. A number of hardware malfunctions in the tape drives have prevented us from using them up to this point.

2. Software Work

The UNIX graphics software has been modified to add new commands and to speed up picture processing. Most of the changes were necessitated by the new seismic data analysis software being developed. The Fortran graphics subroutines have been rewritten in C to simplify software maintenance. The translation has been made possible by a new program which translates C-object modules to Fortran-object modules. This change also clears the way for a slight change in the graphics system design. It will now be possible to fully utilize the inter-process communication ports without the limitations put on them by our Fortran system. The graphics

daemons will now be created when a user invokes a graphics command rather than during system startup. The daemons will also terminate when the user's program terminates. In essence, the user will temporarily be the owner of the graphics daemon while he is using it. There are several advantages to this scheme. There will be fewer processes permanently in the system. It will be easier to specify data files to the graphics daemons without giving complete path names. This and other graphics improvements are a continuing effort.

Heavy usage of the ARPANET software has revealed several bugs both inside and outside the UNIX kernel. A number of these bugs have been fixed, but a number still remain – particularly two bugs in the UNIX kernel which still cause occasional systems crashes. In addition, the FTP code could use some more work and the SERVER TELNET program should probably be completely rewritten.

<div align="right">J. Sax</div>

B. PDP-11 SYSTEM SOFTWARE

During the last six months, we have worked to stabilize our system software and our maintenance procedures, and to prepare the system for export to places such as the VELA Seismological Center. We have put all system sources on-line and carefully checked to see that these sources match the binaries we are using. In a number of cases, we have had to get more up-to-date sources because binaries had been imported without sources. We have put the manual on-line and have created system that makes it easy to print manual sections. However, much work needs to be done to update the manual, especially for system maintenance programs.

We have also designed and implemented a set of maintenance programs called the Team Programmer System (TPS). TPS automatically keeps records of changes made, makes backups at the right moments, and performs checks when destroying backups. Using TPS, we expect our system maintenance to be shared with several other separately funded projects inside Lincoln Laboratory, thereby distributing the cost. Each project will provide one or more people who will spend typically 10 to 30 percent of their time making system improvements, with all projects then sharing these improvements. This concept, which is slowly evolving, will be initially tested when another project brings up a PDP-11/70, using our software.

<div align="right">R. L. Walton
P. A. Neilson</div>

C. DATACOMPUTER-RELATED UNIX SOFTWARE

The previous SATS[1] described our plans to develop software that would automatically create Datacomputer files containing associated waveforms for selected events chosen from the PESF (Preliminary Event Summary File). The first version of this software has been completed and has been run on a test basis for a period of two weeks. The tests revealed that the software operated correctly, but the Datacomputer response was unacceptably slow.

With the aid of the user support services of the Computer Corporation of America (CCA), who are responsible for maintaining the Datacomputer, we have analyzed the reasons for this slowness and have identified a possible solution. The first version of our software issued a separate Datacomputer request for each waveform segment to be extracted from the raw data files and moved to our own waveform files. With 11 SRO stations presently available, and a potential of 1 short-period and 3 long-period waveforms per station, this resulted in up to 44 separate requests for each event processed. There are at least two sources of Datacomputer

overhead associated with each request – compiling the request and accessing the data files referred to by each request. It appears that the latter is the main source of our problem.

CCA suggested two ways we might reduce the request overhead: (1) to group multiple requests into a single request, and (2) to start using a new Datacomputer feature not previously available – precompiled requests. Both these changes involved rewriting the request in its general form and then transmitting the parameters of each waveform transfer to the request as if they were data. Because the short- and long-period raw-data files differ in format, the easiest way to handle this is to group all the short-period requests for an event into a single request and all the long-period requests for the event into a second request. Requests for waveform segments that overlap day boundaries are not grouped with the others because of their more-complicated format and the fact that such requests do not occur very often.

Dealing with these grouped requests is more complex than dealing with single requests. With single requests, the software only had to deal with success or failure of the entire request. With the group requests, the software must be able to handle more-complicated situations and determine which parts of the request succeeded and which parts failed. Recovery after network failures is similarly made more difficult.

When it became apparent that major modifications were needed before the waveform system became operable, we decided to improve our interim system for retrieving SRO data from the Datacomputer. The existing program to retrieve data, DCREAD,[1] requires the user to input the actual time segment of data to be retrieved. In practice, the seismologists find it more convenient to work with lists of events rather than lists of stations and time segments. Therefore, we have developed software to convert event lists to a properly formatted DCREAD input file. A program to do this for short-period data (DCRISP) has been completed, and a long-period version will follow.

The event list used by DCRISP is in the format of the Bulletin lists that are regularly obtained from the Datacomputer Preliminary Event Summary Files. The second input to DCRISP is a file which contains the station name and the start and stop times of each segment of SRO short-period data stored on the Datacomputer. These short-period detection files are produced by a Datacomputer program that we run each time new SRO data are available. (Since long-period data are stored continuously, we will not need a corresponding file for long-period data.)

Before calling DCRISP, the user may edit his copy of the event list so that it contains only those events in which he is interested. For each event, DCRISP will compute the short-period arrival time at each SRO station. Before adding each data request to the DCREAD input file, it will check each arrival against the short-period detection file and only retain the requests for which data are actually available. In addition to creating a DCREAD input file, DCRISP will also pass the original event information to an event file in the output waveform database.[2] Before actually retrieving the data from the Datacomputer, the user may edit the DCREAD input file to further select out signals from particular stations or with particular distances or azimuths from the event.

<div align="right">

L. J. Turek
P. A. Neilson

</div>

D. UNIX SIGNAL DISPLAY PACKAGE

Since the last SATS,[1] we have released the first version of the general-purpose interactive seismic Signal Display Package (SDP). This program will produce a default display of any

UNIX waveform database and allow the user to modify the display using a set of display change commands.

All the change commands described in the previous SATS,[1] except setting markers at cursor locations, plus a few others not mentioned are available in this release of the SDP. The change commands available in this version allow the user to rescale the data in both x and y, move the waveforms left, right, up, or down, change the separation, return the display to the beginning of the waveform, change whether the data should be displayed clipped or not clipped, and allows the display to be truncated to half the width or expanded back to the full width of the screen.

The truncate command is useful to speed the plotting process when only a short segment of the waveform is of interest. It is also useful when using the special command which allows calling other UNIX programs. Truncating the data to half the screen leaves room for typed input and output on the other half.

The "post" and "unpost" commands are also available. These commands add pieces of associated information to, or remove them from, the picture (after a clear command). The information which can be posted or unposted includes: the waveform itself, the date, time, station name, instrument code, gram file name, comment, amplitude scale, timescale, or a zero line. After each set of change commands, the user may choose to have the changed parts of the display over-written on the existing display, or to have the screen cleared and completely replotted.

Markers can also be displayed, but for now the user must have previously created his own marker file. Work is still being done to allow cursors to be displayed, and markers to be placed at the cursors. This feature will be included when the second version of the SDP is released.

Two special commands have been included in this version. The first, "goback", returns the display to the previous picture. Only one previous display is saved. The second, "!", allows the user to call any of his own programs or UNIX system programs to do waveform processing, make nonstandard modifications to the display, or copy and save current display command files and then return to the display program.

By releasing the current version in its incomplete state, we have been able to get some feedback from the seismologists for improvements and programs to be added to the display package.

When the cursor option is available, we will be able to add features that utilize it, such as a command to align the waveforms according to the cursor and programs which work on windows of data which have been defined by the cursor.

Some special two-pass commands are planned which would delete or add waveforms to the display, reorder the existing waveforms (they are currently displayed in the same order in which they appear in the gram index file[2]), or make a display based only on "posted" waveforms.

One of the new programs planned is a 3-component rotate program which would locate grams that are 3 components of the same instrument and convert them to vertical, radial, and transverse components. Another program will locate grams that are 3 components of the same instrument and assign the same vertical gain to each of them.

We are also trying to make general-purpose programs from programs previously written by the seismologists for their own specific projects. Among these are a filtering program, a decimation program, and an equal gain program to set the gains of all waveforms to an equal value.

To help us in writing these general-purpose programs, we are compiling a package of C-language and Fortran subroutines to make working with the database files easier. We have already provided a set of UNIX commands that can manipulate all files in a waveform database with

a single command. WRM will delete a waveform database, WMV will rename a database (which involves modifying every file that contains references to the database name), and WDUP will duplicate a database under a new name, with the option of forming links to the gram files in order to save disk space.

M. F Patton
L. J. Turek

REFERENCES

1. Seismic Discrimination SATS, Lincoln Laboratory, M.I.T. (30 September 1977), DDC AD-A050584.

2. Ibid. (31 March 1977), DDC AD-A045453/8.

GLOSSARY

ARPANET	DARPA Computer Network
CCA	Computer Corporation of America
CTBT	Comprehensive Nuclear Test Ban Treaty
FTP	File Transfer Protocol
ISC	International Seismological Center
JB	Jeffreys-Bullen (Tables)
LASA	Large Aperture Seismic Array (Montana)
LRSM	Long Range Seismic Measurements
NORSAR	Norwegian Seismic Array
NTS	Nevada Test Site
OBS	Ocean-Bottom Seismograph
PDE	Preliminary Determination of Epicenters
PESF	Preliminary Event Summary File
PNE	Peaceful Nuclear Explosion
SATS	Semiannual Technical Summary
SDP	Signal Display Package
SNR	Signal-to-Noise Ratio
SRO	Seismic Research Observatory
TPS	Team Programmer System
USGS	U.S. Geological Survey
VDH	Very Distant Host Interface
WWSSN	World-Wide Standard Seismograph Network

REPORT DOCUMENTATION PAGE		READ INSTRUCTIONS BEFORE COMPLETING FORM
1. REPORT NUMBER ESD-TR-78-64	2. GOVT ACCESSION NO.	3. RECIPIENT'S CATALOG NUMBER
4. TITLE (and Subtitle) Seismic Discrimination		5. TYPE OF REPORT & PERIOD COVERED Semiannual Technical Summary 1 October 1977 – 31 March 1978
		6. PERFORMING ORG. REPORT NUMBER
7. AUTHOR(s) Michael A. Chinnery		8. CONTRACT OR GRANT NUMBER(s) F19628-78-C-0002
9. PERFORMING ORGANIZATION NAME AND ADDRESS Lincoln Laboratory, M.I.T. P.O. Box 73 Lexington, MA 02173		10. PROGRAM ELEMENT, PROJECT, TASK AREA & WORK UNIT NUMBERS Program Element No. 62701E Project No. 7F10
11. CONTROLLING OFFICE NAME AND ADDRESS Defense Advanced Research Projects Agency 1400 Wilson Boulevard Arlington, VA 22209		12. REPORT DATE 31 March 1978
		13. NUMBER OF PAGES 82
14. MONITORING AGENCY NAME & ADDRESS (if different from Controlling Office) Electronic Systems Division Hanscom AFB Bedford, MA 01731		15. SECURITY CLASS. (of this report) Unclassified
		15a. DECLASSIFICATION DOWNGRADING SCHEDULE

16. DISTRIBUTION STATEMENT (of this Report)

Approved for public release; distribution unlimited.

17. DISTRIBUTION STATEMENT (of the abstract entered in Block 20, if different from Report)

18. SUPPLEMENTARY NOTES

None

19. KEY WORDS (Continue on reverse side if necessary and identify by block number)

seismic discrimination	surface waves	NORSAR
seismic array	body waves	ARPANET
seismology	LASA	

20. ABSTRACT (Continue on reverse side if necessary and identify by block number)

This report describes 23 investigations in the field of seismic discrimination. These are grouped as follows: regional seismic studies (13 contributions), miscellaneous studies (6 contributions), and recent developments in our data and computer systems (4 contributions).

DD ＦＯＲＭ 1473 EDITION OF 1 NOV 65 IS OBSOLETE
1 JAN 73